Review and comparison of tacholess instantaneous speed estimation methods on experimental vibration data

Review and comparison of tacholess instantaneous speed estimation methods on experimental vibration data

Cédric Peeters[a,*], Quentin Leclère[b], Jérôme Antoni[b], Peter Lindahl[c], John Donnal[d], Steven Leeb[c], Jan Helsen[a]

[a] *Vrije Universiteit Brussel, Department of Mechanical Engineering*
[b] *Univ Lyon, INSA-Lyon, Laboratoire Vibrations*
[c] *MIT, Research Laboratory of Electronics*
[d] *United States Naval Academy, Weapons & Systems Engineering Department*

Abstract

Instantaneous speed estimation has become a key part of many condition monitoring procedures for rotating machinery. The ability to track the rotational speed of a system is a critical requirement for the majority of vibration-based condition monitoring methods. Information about the speed enables compensating for potential speed variations that would otherwise impair conventional frequency-based methods. The problem of instantaneous speed estimation based on the vibration signals themselves is one that has received a significant amount of attention in recent years. Installing encoders or tachometers has become a lot less attractive due to the potential cost savings that can be obtained by simply utilizing an accelerometer instead. However, trying to find a speed estimation method that fits a certain application "best" is not so straightforward if one inspects the available literature. It turns out that there are many articles that present slight variations or extensions to already existing techniques. This paper targets a general overview of the available knowledge regarding vibration-based speed estimation techniques. It also aims to review some of the most commonly used techniques by means of a performance comparison of seven speed estimation methods on three different experimental data sets. The resulting speed estimation data of all tested methods is made publicly available such that it can help in forming a benchmark for future speed estimation methods.

Keywords: Tacholess, Speed estimation, Phase demodulation, Multi-order probabilistic approach, Teager-Kaiser Energy Operator, Maximum tracking, Vold-Kalman filter

1. Introduction

Nowadays, vibration analysis has become one of the primary tools in condition monitoring of rotating machinery. While the implementation of monitoring and diagnosis schemes is advancing[1, 2], there are still major scientific improvements to be made for it to evolve into a fully mature

*Corresponding author

Email addresses: cedric.peeters@vub.be (Cédric Peeters), quentin.leclere@insa-lyon.fr (Quentin Leclère), jerome.antoni@insa-lyon.fr (Jérôme Antoni), lindahl@mit.edu (Peter Lindahl), donnal@usna.edu (John Donnal), sbleeb@mit.edu (Steven Leeb), jan.helsen@vub.be (Jan Helsen)

[1] Pleinlaan 2, Elsene, Belgium
[2] F-69621, Villeurbanne, France
[3] 77 Massachusetts Ave, Cambridge, MA 02139, USA
[4] 105 Maryland Avenue, Annapolis, MD 21401, USA

technology. Many analyses are currently still being done manually by a domain expert and often the available knowledge with which decisions regarding maintenance are made, is far from complete. Therefore, understanding the machine and component behavior is essential to advance the signal processing and data analysis methodologies used in condition monitoring.

One of the problems that has received a lot of attention over the past two decades is the presence of speed variation in measured vibration signals. The importance of an accurate speed estimation scheme is underlined by the existence of a special issue on Instantaneous Angular Speed processing and angular applications in the Journal of Mechanical Systems & Signal Processing [3] and of a conference dedicated solely to condition monitoring in non-stationary operations. There is also quite a large body of literature on instantaneous frequency estimation in the field of signal processing. However, the estimation of instantaneous speed from vibration signals addresses a more difficult problem, which often jeopardizes the use of these techniques. Typical problems that can occur for the case of instantaneous frequency estimation from vibration signals are:

- Extremely low signal-to-noise ratio
- Strongly colored noise
- Harmonic interference (a special case of the former point)
- Amplification by resonances (e.g. band-pass filtering in signal processing terms)
- Non-persistent and fading harmonics
- Presence of multiple harmonics
- ...

Accurate knowledge of the rotation speed of a machine is necessary to gain insight in the mechanical signatures of the machine components and it is of vital importance to the majority of leading-edge vibration-based condition monitoring techniques. Many rotating machines indeed do not operate at a constant speed but operates at varying speed regimes. Such non-stationary conditions require an efficient and robust way of estimating the instantaneous angular speed (IAS) in order to not invalidate techniques such as order analysis and angular resampling. While in the past this information would typically be measured using an angle encoder on one of the rotating shafts [4, 5, 6], recent research efforts concentrate primarily on extracting the IAS directly from the vibration signal due to the potential cost savings or installation problems. In industry however it is still common practice to use rotary encoders to estimate the speed due to the reliability and the accuracy. A whole range of rotary encoder types exists. Incremental encoders are rotary feedback speed and position transducers that produce coded output, typically in the form of a pulse train with a frequency proportional to the rotation speed. Absolute encoders do not produce pulse trains, but generate binary code that allow estimating the shaft position accurately. Typically, absolute encoders operate using an optical method, such as light sources and photo-sensors in combination with a disk made of regions with different transparency. A downside of this approach is that the photosensors must be mounted close to the rotor disc, and a small tolerance is required at the relative sensor positions [7]. If the working distance of the photosensors can be increased from the actuators, it leads to more flexible applications and this is where vision-based solutions come in.

Computer-vision algorithms have been used in the past for visual tracking of an object [8], examples are techniques such as SIFT [9] and SURF [10]. Vision-based methods are applicable for objects positioned relatively far from the observer and thus do not have the same structural limitation as standard optical encoders. Nowadays, there are quite a few publications available that investigate rotation speed measurement using vision-based methods [11, 12, 13, 14, 15]. Each paper suggests different approaches in tracking the rotation speed and angle, but most of them are based on tracking high-contrast markers or speckle patterns. Typically this involves using ex-

pensive camera equipment capable of filming at very high frame rates. Recently, Zhong et al. [16] showed that artificial fringe patterns and linear array sensors can be employed to estimate with high precision the instantaneous rotational speed. Following the Industry 4.0 trend, there is an increasing focus on cost efficiency also in this research field. Wang et al. [17, 18] show that vision-based rotation speed estimation is feasible using a low-cost imaging device. Their methodology is based on tracking the degree of similarity, quantified by a two-dimensional correlation, between consecutive images. The periodicity of the low-resolution similarity can then be exploited using the Chirp-Z Transform. While these low-cost, vision-based encoders do not achieve the same accuracy yet as the standard optical encoders, this deficit will certainly decrease in the future when imaging sensors become even cheaper and algorithms more optimized.

Currently, the main benefit of using a direct speed measurement approach, i.e. an angle encoder, as compared to an indirect approach, i.e. vibration-based speed estimation, is still the accuracy. When using an indirect method such as vibration-based speed estimation, the analysis is often confronted with several interfering sources due to the nature of the vibration measurements, e.g. resonances, non-speed related harmonics, noise, etc. These effects can have a detrimental effect on the accuracy as compared to angle encoders. On the other hand, vibration sensors are often cheaper and easier to install than angle encoders. Sometimes it can be unfeasible to instrument the shaft of interest with a standard encoder when the shaft is too large or not accessible. Also the data acquisition system needs to be capable of reading in and processing the encoder data stream and often requires dedicated measurement hardware. The capability to simultaneously measure the vibrations for condition monitoring purposes and estimate the speed based on those vibrations allows to circumvent the encoder-related practical inconveniences and costs.

This paper focuses on estimating the IAS based on the information contained within the vibration signal. While it is possible to utilize the IAS itself as a form of indicator for the condition of the machine, this typically involves installing a high-resolution encoder [19, 20, 21] in order to reach the required accuracy of the IAS to be able to detect small faults. Analyzing signals in the angular domain is one of the main reasons why most condition monitoring procedures include speed estimation. Even though there have been many publications in the past decade detailing various “encoder-less” or “tacholess” speed estimation methods, most of them can be categorized into a limited amount of groups.

A large number of contributions focuses on extracting speed information by tracking harmonics in a time-frequency representation (TFR) of the vibration signal with varying degrees of complexity. Typical examples of such TF representations are the short-time Fourier transform (STFT), the wavelet transform, or a Wigner-Ville distribution. Urbanek et al use a simple maximum tracking in the spectrogram in a comparison with phase-based demodulation methods [22]. Furthermore, multiple research papers investigate the possibility to improve the STFT for instantaneous frequency tracking by increasing the resolution when necessary. Kwok et al. [23] implement an adaptive short-time Fourier transform that chooses the optimal window parameters based on an entropy concentration measure of the STFT. Cheung et al. [24] use two kernel functions of different supports to obtain a wideband and a narrowband spectrogram. To preserve the localization characteristics, they implement a combined spectrogram using the geometric mean of the corresponding STFT amplitudes. Peng et al. [25] use a chirplet transform with a polynomial kernel to extend the standard chirplet transform to non-linear IAS estimation with improved frequency resolution. Sekhar et al. [26] investigate the effect of interpolation on the polynomial Wigner-Ville distribution and

IAS estimation. An alternative to the STFT that is often used when more flexibility regarding frequency and time resolution is required, is the wavelet transform. Gryllias et al. [27] use complex shifted Morlet wavelets to find the optimal shift and bandwidth from which to determine the instantaneous speed. Current signals can also use this type of techniques to determine the speed since they are very similar to vibration signals. Aller et al [28] use an analytic wavelet transform on the stator current signal of an AC machine combined with a simple ridge tracking algorithm.

A fairly recent development is the synchrosqueezing transform. In 2009, Daubechies et al. [29] proposed this new technique in the context of audio analysis. Generally, it can be considered as a special type of reassignment method, similar to what had been done before for the STFT and other conventional TFRs [30, 31]. The purpose of this type of reassignment techniques is to improve the concentration of signal components in the time-frequency plane making them more suitable for visual analysis and for methods such as ridge extraction. Correspondingly, there has been a surge in papers making use of the advantages of this new technique [32, 33, 34]. Xi et al. [34] propose a frequency-shift synchrosqueezing algorithm to generate the TFR that afterward gets used as input for the Viterbi algorithm to find the IAS. Shi et al. [32] employ a step-wise demodulation transform in combination with STFT-based synchrosqueezing to determine the IAS. However, there is still strong concern about whether or not synchrosqueezing actually increases the reliability of speed tracking on noisy multi-component vibration signals [35, 36, 37] compared to an STFT or Wavelet transform. Considering this concern and to keep the length of the paper limited, synchrosqueezing is not investigated in this paper.

Other papers focus more on improving the tracking in a TFR rather than improving the TFR itself. Barrett et al.[38] use Hidden Markov Models to incorporate probability in the evolution of the instantaneous frequency. Schmidt et al. [39] incorporate a priori probabilistic knowledge about the instantaneous frequency of the system to increase the robustness of the maxima tracking in the STFT. Quite a few papers focus on implementing a robust ridge detection scheme to track the IAS [40, 41]. The TFR used for ridge detection varies based on the application and sometimes also based on the preference of the authors, but most of them take into account some a priori knowledge about the physical system under investigation. Wang et al. [41] propose the non-linear squeezing time-frequency transform in combination with ridge detection to estimate the IF. Iatsenko et al. [42] use an improved dynamic path optimization method to efficiently estimate the candidate path that best represents the IAS. They also investigate the applicability and performance of their method on different TFRs such as the STFT, the Wavelet transform, and their synchrosqueezed variants.

Some techniques try to utilize more than just one single harmonic present in the signal and its TFR. These methods try to make full use of all the mechanical events linked to the speed, e.g. all synchronous gear and shaft harmonics in a gearbox. Often in complex rotating machinery, there are different operating regimes, potentially leading to other harmonics to be excited or to significant amplitude differences of the tracked harmonics. Therefore, the idea of using multiple harmonics makes sense for the purpose of increasing robustness. For example Zimroz et al [43] divide the STFT into different frequency sub-bands belonging to different harmonic orders and detect the instantaneous meshing frequency for each of the orders by modeling the noise levels and using a threshold based on the spectral kurtosis. Afterward they perform an averaging of the different normalized instantaneous meshing frequencies to obtain a mean estimate of the speed. A fairly recent development is the multi-order probabilistic approach [44, 45]. This approach does not require a priori knowledge about the exact harmonic related to a certain periodic mechanical event but views the STFT as a probability density function (pdf) map of the speed. These multi-

harmonic methods perform particularly well when the harmonic structure of the signal is well known and excited.

Another major group of speed estimation methods makes use of band-pass filtering and phase demodulation based on the analytic signal. Usually one speed-related harmonic is selected based on its signal-to-noise ratio (SNR) and then used for phase demodulation after band-pass filtering around that harmonic [22, 46, 47, 48]. There are also multiple different ways to obtain the demodulated phase. Bonnardot et al. [46] introduced the standard demodulation approach as described above in order to angularly resample the vibration signal and they indicate some considerations and limitations about the technique. Boudraa et al. [49] use the Teager Energy Operator in combination with Empirical Mode Decomposition to obtain instantaneous frequency (IF) estimates for every Intrinsic Mode Function (IMF). This approach does rely on the assumption that each IMF corresponds to a band-pass filtered, IF-related harmonic. A unique approach related to demodulation was proposed by Randall et al. [50] based on a new interpretation of the Teager Kaiser Energy Operator (TKEO). It avoids issues one might get with unwrapping the phase in the standard phase demodulation approach and is based on utilizing amplitude demodulation in the form of the squared envelope of the band-pass filtered signal.

Lastly, there are a number of lesser used approaches for speed estimation. Cardona et al. [51] use a square-root cubature Kalman filter to estimate the speed and for order tracking of the signal. They estimate the number of orders necessary for the Kalman filter based on the number of high amplitude harmonics. Scala et al. [52] use an extended Kalman filter non-stationary sinusoid tracker (EKF-NST) that also allows for both frequency estimation and order tracking. The downside of most model-based approaches is that they require a lot of input parameter tweaking which is often difficult to automate. Another unique approach is based on the scale transform. Combet et al. [53] use a short-time scale transform to estimate the instantaneous speed relative fluctuation based on the varying time-scale factor along the vibration signal.

The idea behind this paper is to assess the advantages, disadvantages, and performance of these different types of techniques. Based on the available literature, it is clear that there are a lot of possible variations on the same methods out there, resulting in often very similar speed estimation techniques. Since it is impossible to implement and test all of these variations, a selection is made from the different groups mentioned earlier to provide a qualitative comparison. The techniques are examined for their performance on three experimental data sets originating from three different machines, namely a wind turbine gearbox, an aircraft engine and the generator of a ship.
The authors hope that for people interested in instantaneous speed estimation, this paper will provide a clear overview of the (dis)advantages of each approach such that they do not have to guess which approach fits their application or needs the best, which is often the case for newcomers to this field. The performance comparison on the three data sets is meant to corroborate the findings. Not only the accuracy of the end result is taken into account, but also things that are more related to the ease of use of the method, like the ease of implementation, the computation time, the number of input parameters and the sensitivity to those input parameters.

2. Methodology

The methods compared in this paper are in essence either based on demodulation or on a time-frequency representation of the signal, since these represent the majority of the techniques out there. This means that no purely model-based or scale transform approaches are investigated. In total seven methods are assessed:

1. Phase demodulation

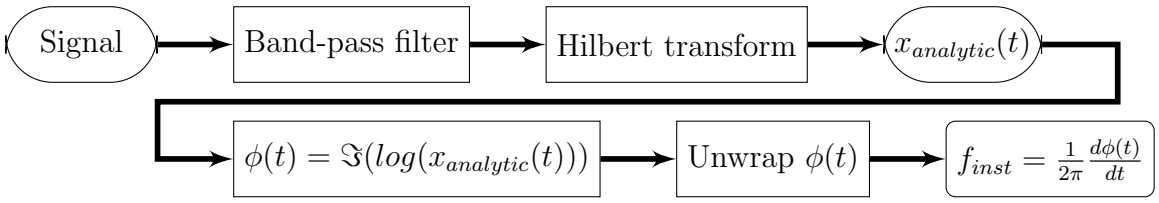

Figure 1: Overview of a standard phase demodulation approach.

2. Iterative phase demodulation
3. Demodulation based on the Teager-Kaiser Energy Operator
4. Multi-order probabilistic approach
5. ViBES method
6. Cepstrum-based multi-order approach
7. Maximum tracking in combination with a Vold-Kalman filter

A short background summary of every method is provided to explain some of the key details concerning the methods. For more detailed information, interested readers are referred to the origin articles of each method, with the exception of the ViBES method which has not been published before. Keep in mind that some of the techniques presented here can also be used in different combinations with other techniques, but investigating all possible combinations would be unfeasible.

2.1. Phase demodulation based on analytic signal

Perhaps the most used approach for vibration-based instantaneous angular speed estimation is based on phase demodulation of a shaft-speed related harmonic that exhibits a high signal-to-noise ratio. This method is fairly straightforward and is mainly based on using an (ideal) band-pass filter around a well-separated, high SNR harmonic of the rotation speed. After defining the optimal lower and upper cutoff frequencies for the band-pass filter, the harmonic is isolated from the complex spectrum. Next, the analytic signal $x_{analytic}(t)$ can be obtained by inverse Fourier transforming the complex band-pass filtered spectrum to the time domain without its negative frequencies. This $x_{analytic}(t)$ is then ideally a mono-component signal with a high SNR and can be written in its exponential form:

$$x_{analytic}(t) = A(t)e^{j\phi(t)} \; with \; A(t) \geq 0 \tag{1}$$

Thus, the instantaneous phase is given by the imaginary part of the logarithm of the analytic signal:

$$\phi(t) = \Im(log(x_{analytic}(t))) \tag{2}$$

Finally, the instantaneous frequency is estimated based on the variation of the unwrapped phase:

$$f_{inst}(t) = \frac{1}{2\pi}\frac{d\phi(t)}{dt} \tag{3}$$

The instantaneous angular speed can then be obtained by multiplying $f_{inst}(t)$ with the correct kinematic ratio.

Figure 1 shows a flowchart of the full approach that clearly does not require a lot of steps and is easy to implement.

While this approach can deliver very accurate IAS estimations in cases where such a single, constantly present, and dominant harmonic is existing, there are ample cases where this approach has its limitations regarding applicability. In complex rotating systems, the deterministic components

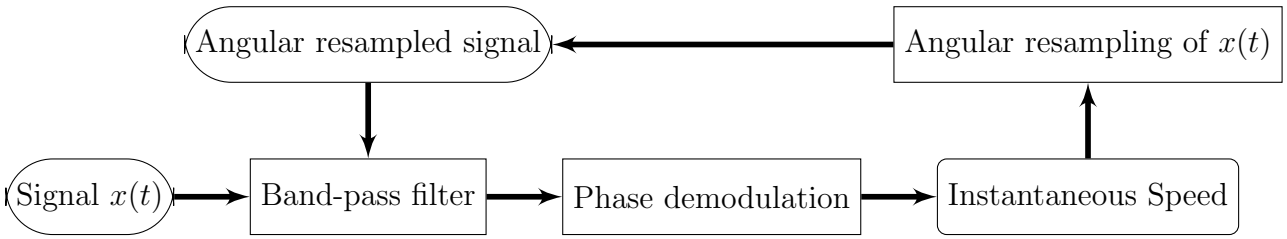

Figure 2: Overview of the iterative demodulation approach.

are not necessarily all harmonically related, causing crossing orders and skewing the extracted instantaneous phase. Additionally, such systems often operate in strongly varying conditions which can cause harmonics to fade into the noise. Another limitation of this technique is the boundaries for the possible speed fluctuation. When a harmonic at a higher frequency is chosen, this often accompanies a reduced possible relative bandwidth size for the band-pass filter due to overlapping of lower and higher order harmonics. Take for example the straightforward case where there are only harmonics of the shaft speed present in the signal at frequency f_{shaft}, so no sidebands related to the meshing of gears. The maximum speed fluctuation $\Delta\dot{\theta}_{max}$ that can be present in the signal to allow for band-pass filtering the n$^{\text{th}}$ harmonic so that it does not overlap with its lower order harmonic at $(n-1)$ and higher order harmonic at $(n+1)$ is:

$$\Delta\dot{\theta}_{max} = \frac{f_{shaft}}{2n+1} \tag{4}$$

with f_{shaft} being the average of the minimum and maximum shaft speed. This means that in order to define a band-pass filter on the second harmonic $n = 2$ so that it does not overlap with the third harmonic, the speed fluctuation of the signal cannot be greater than $\frac{f_{shaft}}{5}$.

This simple example shows that the possible speed fluctuation quickly gets limited by the maximum bandwidth that does not cause overlap with other harmonics. A small adaptation of the method is therefore made for long signals with strong speed fluctuations. For such signals, it is impossible to incorporate the full signal in one demodulation step since the required filter bandwidth would be too large and encompass multiple harmonic orders. Thus the demodulation is done consecutively on windowed sections of the signal. In this paper a rectangular window with a standard overlap of 50% is chosen for all phase demodulation methods. The obtained speed profiles of overlapping sections are averaged together using a weighted average based on a Hanning window with its center in the middle of the window. This is done to reduce the influence of the end effects associated with using an ideal FFT band-pass filter.

2.2. Iterative phase demodulation

The previous paragraph touches upon the fact that it is not always possible to define a band-pass filter on the full signal when the speed fluctuation is too high. Therefore, a possible remedy [54] is to use a lower order harmonic first. This way an initial speed estimate can be obtained which can afterward be used for angular resampling of the signal. After angular resampling, the speed fluctuation still present in the signal is due to the estimation error in the initial speed estimate, but it should have greatly decreased. Thus, another phase demodulation step can be performed using a higher order harmonic now with a band-pass filter that has a smaller bandwidth thanks to the decreased speed fluctuation. Figure 2 shows a simplified diagram of this iterative demodulation approach.

2.3. Teager-Kaiser Energy Operator

An interesting new way of looking at the Teager Kaiser Energy Operator (TKEO) was found by Randall et al. [50]. Instead of using the TKEO for tracking the energy in speech signals, they show that it is possible to estimate the speed directly from the TKEO formulation.

The TKEO is defined in continuous form as follows:

$$\Psi_c(x(t)) = [\dot{x}(t)]^2 - x(t)\ddot{x}(t) \tag{5}$$

If the TKEO is applied to a monocomponent signal such as an amplitude and frequency modulated sine (which in practice can be achieved through band-pass filtering), then the signal $x(t)$ can be written as:

$$x(t) = A(t)sin(\phi(t)) \; with \; \phi(t) = \int_t \omega(t)dt \tag{6}$$

with $A(t)$ and $\omega(t)$ = the time-dependent amplitude and frequency respectively. If the variation of these two quantities is slow, then:

$$\dot{x}(t) \approx \omega(t)A(t)cos(\phi(t)) \tag{7}$$
$$\ddot{x}(t) \approx -[\omega(t)]^2 A(t)sin(\phi(t)) \tag{8}$$

The TKEO then becomes:

$$\Psi_c(x(t)) = [\dot{x}(t)]^2 - x(t)\ddot{x}(t) \tag{9}$$
$$\approx [\omega(t)]^2[A(t)]^2(cos^2\phi(t) + sin^2\phi(t)) \tag{10}$$
$$\approx [\omega(t)]^2[A(t)]^2 \tag{11}$$

The squared envelope $se_x(t)$ of $x(t)$ is defined as:

$$se_x(t) = x^2(t) + \hat{x}^2(t) \tag{12}$$

with $\hat{x}(t)$ the hilbert transform of $x(t)$. It then follows that:

$$\Psi_c(x(t)) = [\omega(t)]^2[A(t)]^2 = [\omega(t)]^2 se_x(t) = se_{\dot{x}}(t) \tag{13}$$

$$\omega(t) = \sqrt{\frac{se_{\dot{x}}(t)}{se_x(t)}} \tag{14}$$

As Randall et al. point out in their paper [50], it is quite straightforward to implement this technique. A zero phase-shift ideal FFT filter can be used to band-pass filter the signal. The squared envelope $se_x(t)$ is obtained by simply inverse Fourier transforming the filtered band back to the time domain without the negative frequencies and squaring the amplitude. The squared envelope of the derivative $se_{\dot{x}}(t)$ is obtained in exactly the same way but an additional multiplication with $j\omega$ is done in the spectral domain concurrently with the band-pass filtering. Multiplying with $j\omega$ is equivalent to applying an ideal differentiation filter on the signal. It avoids partially the typical differentiation issue related to noise amplification of higher frequencies (due to the differentiation filter gain that increases linearly with frequency) thanks to the limited bandwidth of the band-pass filter. The use of ideal Fourier filtering does create some end effects related to the Gibbs phenomenon, but these can be alleviated if one can transform a slightly larger signal part. The start and the end of the signal can then simply be discarded in further analysis.

2.4. Multi-order Probabilistic approach

The multi-order probabilistic approach (MOPA) belongs to the group of techniques that try to utilize more than just one harmonic order in the signal for the speed estimation. The general idea behind MOPA as proposed by Leclère et al. [44] is based on regarding the instantaneous spectrum, which can be obtained through a short time Fourier transform (STFT), of the vibration signal as a probability density function (pdf) of the IAS Ω. Consequently, if the spectrum has a high amplitude at frequency f, there is a high probability that the shaft frequency is equal to f/H_i with H_i being the excitation order or, for the cases described below, the gear ratios. The STFT can be calculated for a signal $x(n)$ as follows:

$$STFT_x(m,k) = \sum_{n=0}^{N-1} x(n)w(n-m)e^{-2\pi jk\frac{n}{N}} \tag{15}$$

with N the window length, n the sample index, m the window index, and k the frequency index. It is important to define a range for the IAS in which the user expects the IAS to reside. This range has a lower bound Ω_{min} and an upper bound Ω_{max}. The following pdf can then be constructed:

$$\begin{cases} p(\Omega|H_i) = \frac{1}{\xi_i}A(H_i\omega) & \text{for } \Omega_{min} < \omega < \Omega_{max} \\ p(\Omega|H_i) = 0 & \text{for } \omega < \Omega_{min} \text{ — } \omega > \Omega_{max} \end{cases} \tag{16}$$

with $A(f)$ a whitened version of the vibration signal's spectrum and ξ_i a normalization factor to make sure the pdf has unit area:

$$\xi_i = \int_{\Omega_{min}}^{\Omega_{max}} A(H_i\omega)d\omega. \tag{17}$$

The purpose of the whitening is essentially to reduce the influence of resonances on the generated pdf, since it is undesirable to give a too high probability to a certain part of the spectrum only due to the increased amplitudes because of a resonance. The used whitening technique should be chosen based on the application.

To improve the IAS estimation and utilize more of the information potential of the spectrum, one has to include more than just one pdf based on one gear ratio or meshing order. Afterwards these different pdfs can be combined together in one pdf by multiplication. Equation 16 does not take into account the possibility that a part of the spectrum for a certain harmonic H_i can exceed the Nyquist frequency. In this case the pdf is made uniform above f_{max}/H_i:

$$\begin{cases} p(\Omega|H_i) = \frac{1}{\xi_i}A(H_i\omega) & \text{for } \Omega_{min} < \omega < f_{max}/H_i \\ p(\Omega|H_i) = \frac{1}{\Omega_{max}-\Omega_{min}}p(\Omega|H_i) = 0 & \text{for } \omega < \Omega_{min} \textit{ or } \omega > \Omega_{max} \end{cases} \tag{18}$$

with ξ_i now:

$$\xi_i = \frac{\Omega_{max} - \Omega_{min}}{f_{max}/H_i - \Omega_{min}} \int_{\Omega_{min}}^{f_{max}/H_i} A(H_i\omega)d\omega. \tag{19}$$

The inputs of the method are thus an approximate range for the IAS, the meshing orders and the vibration signal. For every order a pdf is then constructed based on the signal's instantaneous spectrum and rescaled to the given range for the IAS. Next, the pdfs are multiplied to combine the information of all the orders so that the main corresponding estimate for the IAS becomes the most dominant peak in the pdf.

Currently, the pdfs are still independently generated for each time step and thus do not guarantee any continuity of the IAS, which is a logical assumption for any mechanical system. Due to the inertia of the rotating shafts, strong acceleration or deceleration is improbable. As such, to improve the results further, an a priori of continuity is introduced for the IAS. The concept relies on generating for each time step a pdf that is based on the pdfs of several time steps before and after the central pdf. Appropriate weighting of these pdfs is done by convolving the pdf with a centered Gaussian and the time relationship is introduced by letting the variance depend on the time between the considered pdf and the central pdf. The pdf at time step j generated by the pdf at time step $j+k$ is defined as:

$$p(\Omega_j)_{j+k} = \int_{\Omega_{min}}^{\Omega_{max}} p(\Omega_j|\Omega_{j+k})d\omega \propto \exp(\frac{\omega^2}{2\sigma_k^2}) * p(\Omega_{j+k}) \tag{20}$$

with $p(\Omega_j)_{j+k}$ the pdf at time j that can be obtained by convolution of the pdf at time $j+k$, $p(\Omega_{j+k})$ with a centered Gaussian, and $\sigma_k = |\gamma k \Delta_t|$ with Δ_t being the time step, γ the standard acceleration of the IAS. Similar to the previous step in which the pdfs corresponding to the different orders have to be multiplied for each time step to obtain a single combined pdf, there are now again multiple pdfs for every time step $j+k$ belonging to time steps before and after time step j. Thus the final step is to multiply again all the pdfs for every time step:

$$p(\Omega_j)_s \propto \prod_{k=-K}^{K} [\Omega_j]_{j+k}. \tag{21}$$

The instantaneous angular speed can then simply be obtained by calculating the expected value of every pdf.

2.5. ViBES method

The ViBES method is an STFT-based algorithm recently developed at MIT's Research Laboratory of Electronics and similar in approach to the MOPA method. It also views the STFT as a combination of probability density functions but has the user define ranges of the STFT that represent these pdfs. These ranges also track the instantaneous frequency estimates. For this method, the user defines an initial estimate of the vibration frequency, $\hat{f}_0$, and defines a set of vibration mesh ranges of interest,

$$\mathbf{R} = \{\mathbf{r}_1, \mathbf{r}_2, \ldots, \mathbf{r}_M\}, \tag{22}$$

where $\mathbf{r}_i = [r_{i,\min}, r_{i,\max}]$, i.e., all real values in the range $r_{i,\min}$ to $r_{i,\max}$.

The set of mean values of these ranges,

$$\bar{\mathbf{R}} = \{\bar{\mathbf{r}}_\mathbf{1}, \bar{\mathbf{r}}_\mathbf{2}, \ldots, \bar{\mathbf{r}}_M\} \tag{23}$$

should correspond to strong (in the signal-to-localized-noise ratio sense) individual vibration spectral components correlated to the frequency profile of interest (e.g. the frequency of a particular shaft's rotation). For convenience, these mesh ranges should be ordered from low to high and related such that,

$$\frac{\mathbf{r}_1}{\bar{\mathbf{r}}_1} = \frac{\mathbf{r}_i}{\bar{\mathbf{r}}_i}. \tag{24}$$

In this way, the user can define $\bar{\mathbf{R}}$ based on the expected locations of strong vibrational mesh content, and set the width of all the corresponding ranges based on the width of a single range.

This defining range should be set wide enough so that all ranges sufficiently encompass their corresponding vibrational spectrum component but not too wide that any range also encompasses adjacent correlated vibrational spectrum content. For example, for harmonically related vibration meshes, each range should only encompass one harmonic.

The method operates by calculating the STFT as defined in Eq. 15 and obtaining $A_t[k]$ of the vibration measurement, with t being the time at the center of the window.

At each time instance, t, the algorithm converts the M vibration mesh ranges of interest, $\mathbf{R}$, into frequency ranges as,

$$\mathbf{F} = \hat{f}_{t-\Delta t}\mathbf{R}, \tag{25}$$

where $\hat{f}_{t-\Delta t}$ is the previous time instance frequency estimate. The corresponding M sections of $A_t[k]$ are $A_t[\mathrm{K}]$ where $\mathrm{K} \ni k_i$, and,

$$k_i = N\frac{\hat{f}_{t-\Delta t}}{F_s}\mathbf{r}_i. \tag{26}$$

with F_s being the sample rate of the measurement.

The algorithm treats the magnitude profiles of these M ranges as scaled and sampled probability density function estimates of the location of the vibration frequency profile of interest at time t, i.e.,

$$\hat{p}_{t,i}\left(f_i\right) = \alpha_i |A_t[k_i]|, \tag{27}$$

where,

$$f_i = \frac{f[k_i]}{\bar{\mathbf{r}}_i}. \tag{28}$$

Here, α_i is the scaling factor to ensure $\sum \hat{p}_{t,i}(f_i) = 1$.

If the mesh ranges, $\mathbf{R}$, are ordered from low to high and related according to (24), then each f_i will cover a similar range, though f_M will have the highest frequency resolution. Each probability density function, $\hat{p}_{t,i}(f_i)$ can then be interpolated to match the sample points, f_M, so that the M resulting probability density function estimates $\hat{p}_{t,i}(f_M)$ have the same length and thus can be arithmetically combined to form a single composite probability density function,

$$\hat{p}_t(f_M) = g\left(\hat{p}_{t,i}, f_M\right). \tag{29}$$

For the results presented in this paper, the function $g()$ calculates the joint probability density function assuming each $p_{t,i}$ as independent, i.e.,

$$g(\hat{p}_{t,i}, f_M) = \prod_{i=1}^{M} \hat{p}_{t,i}(f_M). \tag{30}$$

Finally, the frequency estimate for time, t, is calculated as the expected value of the composite probability density function,

$$\hat{f}_t = \sum_{f_i \in f_M} f_i \hat{p}_t(f_i). \tag{31}$$

This process is repeated for the length of the vibration signal $x(n)$ to form the full estimated frequency profile, $\hat{f}$.

2.5.1. Adaptation 1: Illegal Regions

To improve robustness, the ViBES method allows defining "illegal" frequency regions unavailable for the analysis. This helps protect against the amplifying influences of resonances as well as vibration disturbances from extraneous sources, e.g., 50 Hz or 60 Hz "hum" corresponding to the electrical line frequency. These regions can be defined as,

$$\mathbf{Z} = \{\mathbf{z}_1, \mathbf{z}_2, \ldots, \mathbf{z}_L\}. \tag{32}$$

At each time instance, t, if any of the frequency regions of $\mathbf{F}$ (calculated in (25)) overlap with any regions of $\mathbf{Z}$, the algorithm removes the overlapping regions from $\mathbf{F}$ and removes the corresponding mesh range from $\mathbf{R}$. That is, (25) becomes,

$$\mathbf{F} = \left\{ \hat{f}_{t-\Delta t}\mathbf{r}_i \mid \hat{f}_{t-\Delta t}\mathbf{r}_i \cap \mathbf{z}_j = \varnothing \quad \forall \quad \mathbf{z_j} \in \mathbf{Z} \right\}, \tag{33}$$

and $\mathbf{R}$ is updated as,

$$\mathbf{R} = \frac{\mathbf{F}}{\hat{f}_{t-\Delta t}}. \tag{34}$$

The analysis then continues through (26) - (31).

2.5.2. Adaptation 2: Variance-Based Lock-in Tracking

The ViBES method also allows the automated toggling between two modes, *wait* and *track*, in response to a criteria metric. For example, the variance in the composite probability density function,

$$\sigma^2 = \sum_{f_i \in f_M} \left(f_i - \hat{f}_t \right)^2 \hat{p}_t(f_i), \tag{35}$$

can be thought of as a confidence metric of the estimate, $\hat{f}_t$. A low value corresponds to when the individual probability density functions, $\hat{p}_{t,i}\left(f_M\right)$, have high signal-local-noise ratios with content co-aligned in f_M. A high value occurs when the signal-local-noise ratio is low and/or when their vibration content is not well co-aligned. If the previous time-instance estimate of frequency, $\hat{f}_{t-\Delta t}$, is good at time instance t, then σ^2 will be small and the analysis should save the updated estimate. However, if the estimate is poor, then the content will not align well and σ^2 will be high. Thus, maintaining a binary state variable S_t and setting it conditional to σ^2 incorporates an algorithmic decision to start, keep, or stop tracking frequency. That is,

$$S_t = \begin{cases} 0, & \text{if } S_{t-\Delta t} = 0 \text{ and } \sigma^2 > \sigma_l^2 \\ 0, & \text{if } S_{t-\Delta t} = 1 \text{ and } \sigma^2 > \sigma_h^2 \\ 1, & \text{if } S_{t-\Delta t} = 0 \text{ and } \sigma^2 \leq \sigma_l^2 \\ 1, & \text{if } S_{t-\Delta t} = 1 \text{ and } \sigma^2 \leq \sigma_h^2 \end{cases}, \tag{36}$$

where σ_l^2 and σ_h^2 are empirical threshold values with $\sigma_h^2 > \sigma_l^2$. In (36), $S_t = 0$ indicates *wait*-mode and $S_t = 1$ indicates *track*-mode. (31) can then be altered to depend on S_t,

$$\hat{f}_t = \begin{cases} \sum_{f_i \in f_M} f_i \hat{p}_t(f_i), & \text{if } S_t = 1 \\ \varnothing & \text{if } S_t = 0 \end{cases}, \tag{37}$$

so that the profile $\hat{f}_t$ only contains estimates when in *track* mode.

Under this operation, (25) and (26) need to be adapted by replacing $\hat{f}_{t-\Delta t}$ with $f_{t,0}$ as $\hat{f}_{t-\Delta t}$ can take on the null set. By setting $f_{t,0}$ as,

$$f_{t,0} = \begin{cases} \hat{f}_{t-\Delta t}, & \text{if } S_t = 1 \\ f_w, & \text{if } S_t = 0 \end{cases}. \tag{38}$$

where f_w is the initial frequency guess when in *wait* mode and defined by the user.

2.6. Cepstrum-based multi-order approach

This paper investigates the performance of combining the cepstrum transformation with the multi-order probabilistic approach. This technique is inspired by the approach proposed by F. Bonnardot at the data contest [55] of the Surveillance 8 conference which was held at the Roanne Institute of Technology in France. In this contest Bonnardot uses the cepstrum to find an initial estimate for the speed. Instead of a Time-Frequency Representation (TFR), a Time-Quefrency Representation (TQR) is generated based on a short-time cepstrum transform. The technique then makes use of a tracking algorithm based on the maxima of the first five rhamonics in the TQR and based on using linear prediction to find the expected quefrencies.

Background about cepstrum

The complex cepstrum is defined as the inverse Fourier transform of the log spectrum. It can be expressed in terms of the amplitude and the phase of the spectrum:

$$C_c(\tau) = \mathscr{F}^{-1}\{\ln(X(f))\} = \mathscr{F}^{-1}\{\ln(A(f)) + j\phi(f)\} \tag{39}$$

where $X(f)$ is the frequency spectrum of the signal $x(t)$:

$$X(f) = \mathscr{F}\{x(t)\} = A(f)e^{j\phi(f)} \tag{40}$$

By setting the phase to zero in Eq.(39), the real cepstrum can be obtained:

$$C_r(\tau) = \mathscr{F}^{-1}\{\ln(A(f))\} \tag{41}$$

Here, τ is a measure of time, referred to as "quefrency", however it is not defined in the same sense as a signal in the time domain. A peak at a certain quefrency corresponds to the inverse period of a series of periodic harmonics in the spectrum. For example, if the sampling rate of a signal is 20 kHz and the cepstrum displays a quefrency peak at 1000 samples, the peak indicates that there is a family of harmonics present in the spectrum with a spacing of 20 Hz (20 kHz/1000 samples).

An important property of the cepstral domain is that the convolution of two time domain signals can be expressed as an addition of their cepstra. Consider the output signal $y(t)$ of a physical system represented by the convolution of an input signal $x(t)$ and an impulse response h(t) of the system:

$$y(t) = x(t) * h(t) \tag{42}$$

Because of the convolution theorem, this time domain expression transforms into a multiplication in the frequency domain:

$$Y(f) = X(f)H(f) \tag{43}$$

In turn, taking the logarithm of Eq.(43) transforms the multiplication into a sum:

$$\ln(Y(f)) = \ln(X(f)) + \ln(H(f)) \tag{44}$$

Since the Fourier transform is linear, the addition remains valid in the cepstral domain.

$$C(\tau) = \mathscr{F}^{-1}\{\ln(Y(f))\} = \mathscr{F}^{-1}\{\ln(X(f))\} + \mathscr{F}^{-1}\{\ln(H(f))\} \tag{45}$$

This property indicates the possibility to deconvolve a signal if one of the factors is known. As such the logarithmic transformation allows the separation of the influence of the excitation source and the transmission path of the system in the cepstral domain. This property opens up possibilities for modal analysis in the cepstral domain [56], but this is not the focus of this paper.

TQR-based speed estimation

The usage of the cepstrum for speed estimation is slightly different in this paper compared to Bonnardot's approach. Instead of using a tracking approach based on the first five harmonics, the TQR is regarded as a probability density function map of the rhamonic orders similar to MOPA.

The TQR of a signal or Short-Time Cepstrum Transform (STCT) is essentially based on the STFT. The STCT is then simply the inverse Fourier transform of the natural logarithm of the absolute values of every spectrum in the STFT. The amount of windows remains the same:

$$STCT_x(m,\tau) = \frac{1}{N}\sum_{k=0}^{N-1} \ln(|STFT(m,k)|e^{-2\pi j\tau\frac{k}{N}}) \tag{46}$$

with τ the quefrency index. This STCT or "cepstrogram" is then used as input for the same formalism as defined in Section 2.4 for MOPA. The key difference between MOPA on the STFT and STCT is based on the fact that a decrease in rotation speed will actually lead to an increase in the quefrency peak related to that rhamonic order. This means that the STCT looks like it is inverted compared to the STFT. All the frequency intervals defined for the spectra are also inverted since the minimum and maximum expected rotation frequency correspond to the maximum and minimum rotation quefrency respectively.

2.7. Maximum tracking combined with Vold-Kalman filter

The final technique to be investigated is a combination of two commonly employed techniques and is based on the three-step procedure described in [39]. First, the spectrogram of the signal is calculated and used for a maximum tracking procedure. There exist quite a few maximum tracking algorithms, but the one showcased in this paper is the one described in [39]. Second, this initial speed estimate based on the maxima serves as input for the Vold-Kalman filter, which is regarded as a time-varying band-pass filter in this context with the center frequency being the initial speed estimate. Third, the resulting, filtered signal should then be a mono-component signal and thus suitable for phase estimation through its analytic signal.

Maximum tracking

The idea behind maximum tracking is very straightforward: the amplitudes of a speed-related harmonic (or set of harmonics) are tracked over time in the spectrogram in an automated way by simply looking at the peaks (maxima) near the expected frequency and assuming that the found peaks are related to the harmonic to track. The manner in which this automated search and tracking is implemented varies greatly within literature [57] and there still does not seem to be a consensus as to what the optimal approach consists of. Regardless, the approach in this paper (as proposed in [39]) is based on solving a constrained optimisation problem in the form of:

$$\underset{k}{\text{minimize}} \ = -|STFT(n,k)|^2 \tag{47}$$

$$subject\ to\ (k\Delta f - f_c(n))^2 \leq \Delta f_c^2 \tag{48}$$

with f_c the center of the constraint, n the time index, Δf_c the bandwidth of the constraint, k the frequency index, and Δf the frequency resolution. It is assumed that:

$$f_{IF}(n\Delta t) \approx f_{max}(n) \tag{49}$$

with f_{IF} the actual instantaneous frequency of the harmonic to track, Δt the time resolution of the spectrogram, and f_{max} the frequency that corresponds to the maximum amplitude. In order to make the tracking process more robust, the acceleration of the instantaneous frequency (IF) can be taken into account. The Taylor series expansion of the IF gives:

$$f_{IF}(t) = f_{IF}(t-\Delta t) + \Delta t \frac{d}{dt} f_{IF}(t-\Delta t) + \frac{1}{2}\Delta t^2 \frac{d^2}{dt^2} f_{IF}(t-\Delta t) + ... \tag{50}$$

The gradients of the IF are of course unknown (and assumed to be continuous) and the actual f_{IF} is also unknown. Therefore, the gradients are estimated using a simple finite difference scheme based on the previous IF estimates $f_{max}(n-1)$, $f_{max}(n-2)$, etc. Next, it is assumed that:

$$f_{max}(n) = f_{IF}(n) + \nu(n) \tag{51}$$

with ν representing the deviation due to smearing of the STFT and noise in the signal. It is assumed that this deviation has a Gaussian distribution $\nu \sim N(0, \sigma^2)$ so that the estimated IF, f_{max}, can be related to the true IF, f_{IF}, as follows:

$$p(f_{max}(n)|f_{IF}(n), \sigma^2) = \frac{1}{\sqrt{2\sigma^2\pi}} e^{-\frac{(f_{max}(n)-f_{IF}(n))^2}{2\sigma^2}} \tag{52}$$

A model of the true IF $f_{IF,w}$ is used since f_{IF} is unknown. An N^{th}-order polynomial is used for $f_{IF,w}$:

$$f_{IF,w} = w_0 + w_1 t^1 + w_2 t^2 + ... + w_N t^N \tag{53}$$

The polynomial weights $\mathbf{w} = [w_0, w_1, w_2, ..., w_N]^T$ are estimated through a maximum likelihood procedure:

$$\hat{\mathbf{w}} = \underset{\mathbf{w}}{\text{argmax}} \prod_{i=n-N_m}^{n-1} p(f_{max}(i)|f_{IF,w}(i), \sigma^2) \tag{54}$$

with N_m the number of previous time steps taken into account. The maximization of the likelihood function under a conditional Gaussian noise distribution for a linear model is equivalent to minimizing a sum-of-squares error function [58]. This boils down to solving a least squares problem which uses a Moore-Penrose pseudo-inverse. The resulting weights can then be found using following matrix expression:

$$\hat{\mathbf{w}} = (\mathbf{Q}^T\mathbf{Q})^{-1}\mathbf{Q}^T\mathbf{f}_{max} \tag{55}$$

with $\mathbf{f}_{max}$ the $(N_m \times 1)$ vector containing the previous N_m IF estimates, and $\mathbf{Q}$ the design matrix of the polynomial:

$$\mathbf{Q} = \begin{pmatrix} 1 & (n-1)\Delta t & \dots & ((n-1)\Delta t)^N \\ 1 & (n-2)\Delta t & \dots & ((n-2)\Delta t)^N \\ \vdots & \vdots & \ddots & \vdots \\ 1 & (n-N_m)\Delta t & \dots & ((n-N_m)\Delta t)^N \end{pmatrix} \tag{56}$$

In this paper a first order polynomial is used to minimize potential errors in the extrapolation. Also a limited number of previous points N_m is taken into account, namely five, for the cases described in this paper to make sure that the computation time remains acceptable. The method does require estimates at the first time index for the IF and its gradient. The initial gradient is assumed zero and the initial IF estimate is obtained by visual inspection of the spectrogram.

The constrained minimization problem is reformulated using a penalised unconstrained cost function (see [39] for more details):

$$\begin{aligned}\kappa(\rho, n, k) = -|STFT(n,k)|^2 &+ \rho_1 \cdot max[0, (k\Delta f - f_{max}(n-1))^2 - \Delta f_{c1}^2] \\ &+ \rho_2 \cdot max[0, (k\Delta f - f_{IF,w}(n))^2 - \Delta f_{c2}^2]\end{aligned} \tag{57}$$

This cost function is minimized using a brute force approach which is computationally feasible as long as the number of points N_m is not too high. The bandwidth for the tracker is denoted by Δf_{c1} and Δf_{c2}. The parameters ρ_1 and ρ_2 are chosen in such a way that the cost function is dominated by the constraint terms in case the constraints get violated. The estimated IF is then given by:

$$f_{max}(n) = \Delta f \operatorname*{argmin}_k \kappa(\rho, n, k) \tag{58}$$

Vold-Kalman filter

The IF estimate returned by the maximum tracking is still quite rough due to the resolution limitations of the spectrogram. Therefore the Vold-Kalman filter (VKF) is employed as a time-varying band-pass filter with a center frequency based on the IF estimate returned by the maximum tracking. The VKF allows for defining a bandwidth of the band-pass filter such that the provided rough speed does not have to be perfect. The larger the bandwidth however, the more noise and extraneous components are included. The implementation used in this paper is based on the one-pole angular-displacement filter as recommended by [39]. The angular-displacement VKF tries to estimate the envelope of the mono-component signal and should be fairly robust to crossing orders compared to the angular-velocity VKF. To keep the length of this paper limited, the full background of the VKF is not provided here, but interested readers are referred to [39, 59, 60, 61] for more details. Finally, after the VKF, the instantaneous speed estimate is found by using the analytic signal as described in Section 2.1.

3. Experimental applications

The seven methods highlighted in Section 2 are examined for their accuracy and ease of use on three different experimental data sets. One data set originates from a wind turbine gearbox, one from an aircraft engine, and one from a ship generator. Each data set has very different characteristics and thus their analysis can provide some interesting insights into the subtleties of each method. Since each method and data set require new input parameter settings, describing all of them each time would be quite cumbersome. Therefore only the most important settings that change between the different cases are reported and the remaining parameters are displayed in tables. A general overview of all the input parameters per method is provided in Table 1. The list of input parameters per implemented method is undoubtedly subjective since another user might want to add or reduce certain inputs as to increase the flexibility for their particular case. However, the input parameters here are defined from a perspective that each method should be easy to use in an automated manner, thus with the least amount of manual effort possible. By

Table 1: Overview of the input parameters of each method.

	Method name						
Input#	Phase demodulation	Iterative demodulation	TKEO	MOPA	ViBES	Cepstrum-based MOPA	maximum tracking+VKF
1	Fs	Fs	Fs	Fs	Fs	Fs	Fs
2	ω_{init}	ω_{init}	ω_{init}	ω_{min}	N_w	ω_{min}	ω_{init}
3	Bw	Bw	Bw	ω_{max}	N_{FFT}	ω_{max}	Bw_{max}
4	N_w	N_w	N_w	$\{H_i\}$	$N_{overlap}$	$\{H_i\}$	N_w
5		$\{H_i\}$		N_w	$\{R\}$	N_w	N_{FFT}
6				N_{FFT}	$\{Z\}$	N_{FFT}	$N_{overlap}$
7				$N_{overlap}$	σ_l^2	$N_{overlap}$	N_p
8				K_w	σ_h^2	K_w	N_m
9				γ		γ	Bw_{VKF}
10							N_{VKF}

with Fs the sampling rate in Hz, ω_{init} the IF at the first time index, Bw the bandwidth of the band-pass filter, N_w the window size used, $\{H_i\}$ the list of harmonic orders, N_{FFT} the size of the FFT in samples, $N_{overlap}$ the amount of overlap between windows in samples, K_w is the number of windows used for the continuity smoothing in MOPA, γ is the expected acceleration of the IAS in MOPA, $\{R\}$ the set of mesh ranges of interest with each range defined by a minimum and maximum value, $\{Z\}$ the set of illegal frequency regions, σ_l^2 & σ_h^2 the variance threshold values for beginning and stopping track- and wait-mode of ViBES, N_p the order of the polynomial used for maximum tracking, N_m the number of previous time steps taken into account, ρ_1 & ρ_2 are the weights for the penalised unconstrained cost function, Bw_{max} & Bw_{VKF} are the bandwidths for the maximum tracking and the vold-kalman filter respectively, and finally N_{VKF} the order of the vold-kalman filter.

looking at Table 1, it can be noticed immediately that the methods based on the STFT need at least three additional parameters just for the calculation of the STFT. The method with the most required inputs is the combination of maximum tracking with the Vold-Kalman filter since this method is probably also the most complex method to implement out of the seven methods tested.

3.1. Wind turbine gearbox data set

This well-documented data set originated from a diagnosis contest held at the International Conference on Condition Monitoring of Machinery in Non-Stationary Operations (CMMNO) in 2014 [44]. The provided vibration signal was measured on the gearbox housing of a wind turbine near the epicyclic gear train and sampled at 20 kHz. The goal was to estimate the IAS of the high-speed shaft (carrying gear #7 in Fig.3). This estimate was then compared with a reference speed signal measured by an angle encoder. The length of the measurement was approximately 550 seconds. The spectrogram of the full signal can be seen in Fig.4 and is generated using a Hanning window of 1 second with 50% overlap.

3.1.1. Parameter settings

The methods based on phase demodulation mainly need one high SNR, speed-related harmonic as their most important input. In this case, the second harmonic of the planet gearmesh frequency around 55 Hz is chosen due to the good results obtained using it, which is also corroborated by the report in [44]. The bandwidth and window size for this case are set at 8 Hz and 10 seconds respectively. The methods based on the STFT all use the same settings for the STFT:

- uniform weighting window
- Window length of 1 second
- FFT size of 2 seconds (thus 1 second of zero padding)
- Overlap of 95% of the short time window length

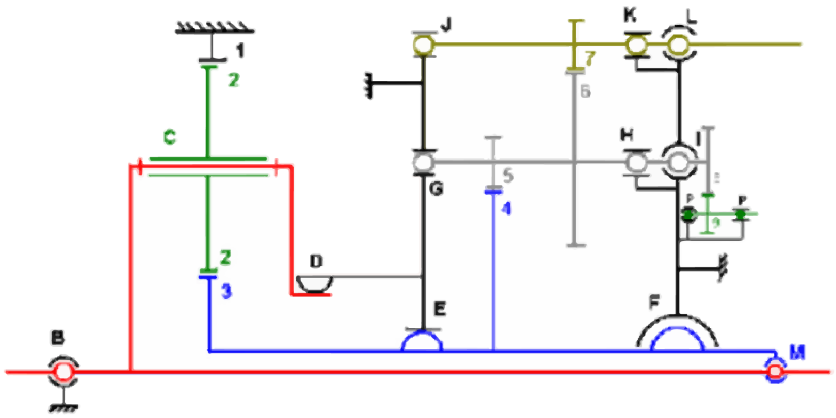

Figure 3: Visualization of the wind turbine gearbox used in the CMMNO 2014 diagnosis contest.

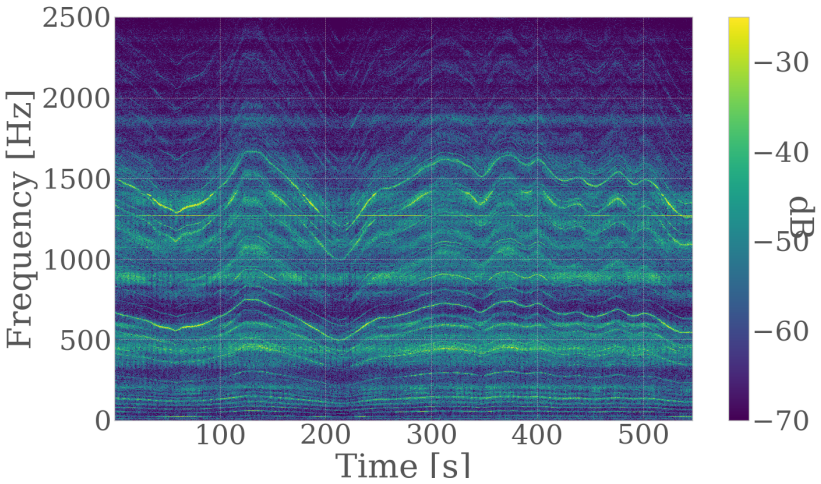

Figure 4: Spectrogram of the CMMNO 2014 diagnosis contest data.

The fundamental harmonic orders taken into account for the multi-order probabilistic approach are displayed in Table 2. The first ten harmonics of every fundamental order are considered for MOPA. The number of windows K_w used for the a priori continuity introduction is set to 20 and the acceleration tolerance of the speed γ is set to 0.4 $\frac{\text{Hz}}{\text{s}}$. The benefit of using MOPA is that it allows the estimation of the speed of the full signal at once. The base frequency interval $\{\omega_{min}, \omega_{max}\}$ used here is chosen to be $\{15, 35\}$. The mesh ranges for the ViBES method are set to $R = \{[0.9290, 1.1219], [1.8580, 2.2438], [2.7871, 3.3657], [4.8167, 5.8167]\}$ and no illegal frequency ranges are defined. The first three of these ranges correspond to the fundamental, and 2nd and 3rd harmonics of the vibration content created by gear pairs 1/2 and 2/3 (Table 2), respectively, while the fourth range corresponds to the fundamental vibration content created by gear pair 4/5 (Table 2).

Finally, for the maximum tracking, the third harmonic of the planet gearmesh frequency which starts at about 75 Hz is chosen for ω_{init}. The bandwidth Bw_{max} is set to 2 Hz, the polynomial order N_p to 1, and the number of previous estimates to take into account N_m to 5. Lastly, the chosen bandwidth Bw_{VKF} is 4 Hz and the VKF order N_{VKF} is 2. An overview of every single

Table 2: Fundamental orders related to high-speed shaft.

Gear pair	**Order value**
1	1
2/3,1/2	1.025459229
4/5	5.316666667
6/7	29
8/9	15.225
10/11	6.619565217

Table 3: Overview of the input parameters for the CMMNO data set

Method name						
Phase demodulation	Iterative demodulation	TKEO	MOPA	ViBES	Cepstrum-based MOPA	maximum tracking+VKF
$\omega_{init} = 53$ Hz $Bw = 8$ Hz $N_w = 50000$	$\omega_{init} = 53$ Hz $Bw = 8$ Hz $N_w = 50000$ $\{H_i\} = \{2, 10.62\}$	$\omega_{init} = 53$ Hz $Bw = 8$ Hz $N_w = 50000$	$\omega_{min} = 15$ Hz $\omega_{max} = 35$ Hz $\{H_i\}$ =Table 2 N_w=5000 $N_{FFT} = 10000$ $N_{overlap}$=95% $K_w = 20$ $\gamma = 0.4\frac{Hz}{s}$	$\omega_{init} = 25$ Hz $N_{FFT} = 2^{14}$ $N_{overlap}$=90% N_w=10000 $\{R\} = \{[0.9290, 1.1219], [1.8580, 2.2438], [2.7871, 3.3657], [4.8167, 5.8167]\}$ $\{Z\} = \{\}$ σ_h^2=[ ] σ_l^2=[ ]	$\omega_{min} = 15$ Hz $\omega_{max} = 35$ Hz $\{H_i\}$=Table 2 N_w=5000 $N_{FFT} = 10000$ $N_{overlap}$=95% $K_w = 20$ $\gamma = 0.4\frac{Hz}{s}$	$\omega_{init} = 75$ Hz Bw_{max}=2Hz $N_w = 5000$ $N_{FFT} = 10000$ $N_{overlap}$=95% N_p=1 N_m=5 Bw_{VKF}=4 Hz N_{VKF}=2

input parameter is shown in Table 3.

3.1.2. Results

Some intermediary results are shown first in order to illustrate better the internal workings of the different methods. As described in Section 2.4, MOPA views the spectrogram as a probability density function (pdf) map and relates all of the pdf intervals belonging to different harmonic orders back to the fundamental speed interval, in this case $\{15, 35\}$. Figure 5 shows the obtained pdf map after summation and continuity introduction for the fundamental speed interval on the CMMNO data. The instantaneous speed profile can then be obtained by taking the expected value of every pdf at every time step.

The same approach is employed for the cepstrum-based MOPA, but the STCT or cepstrogram is used instead of the spectrogram. Figure 6 displays the used cepstrogram with quefrency on the y-axis. The structure of the rhamonics clearly corresponds to the inverse of the instantaneous speed profile. Therefore the obtained pdf map, as shown in Fig. 7, also returns an inverted speed estimate. By taking the expected quefrency values of the pdf map and simply inverting them, the instantaneous frequency values are recovered.

The maximum tracking method basically calculates a 2D cost map based on a penalized unconstrained cost function and the spectrogram. Figure 8 shows the cost map as an overlay in red over the spectrogram in the background. The cost map is red where the cost is very high and becomes more transparent where the cost is low. Clearly, the cost is lowest around the third harmonic of the planet gearmesh frequency since this harmonic lights up through the cost map layer. The input rough speed estimate for the VKF is then acquired by taking the frequency that corresponds to the minimum cost at every time step.

The extracted speed profiles of the seven different methods are then compared to the reference

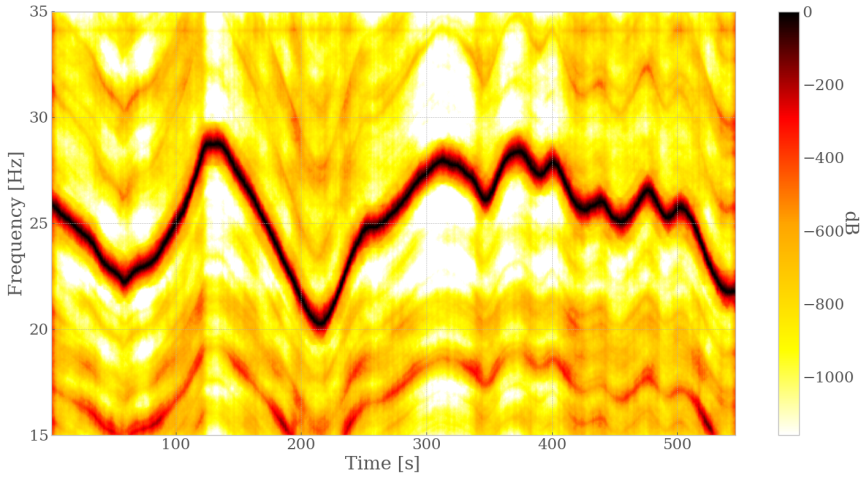

Figure 5: pdf map of the speed profile based on the CMMNO spectrogram after continuity introduction.

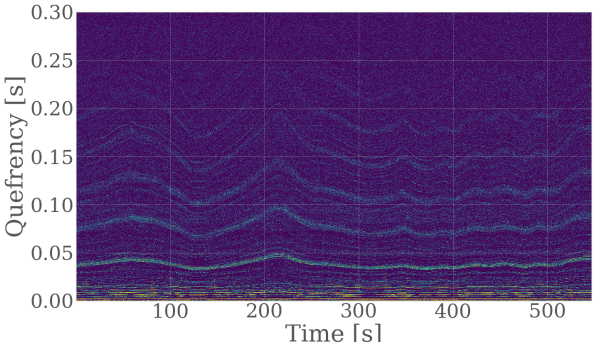

Figure 6: Cepstrogram of the CMMNO data.

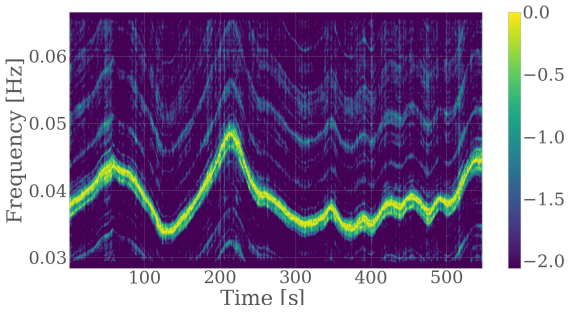

Figure 7: pdf map of the speed profile based on the CMMNO cepstrogram after continuity introduction.

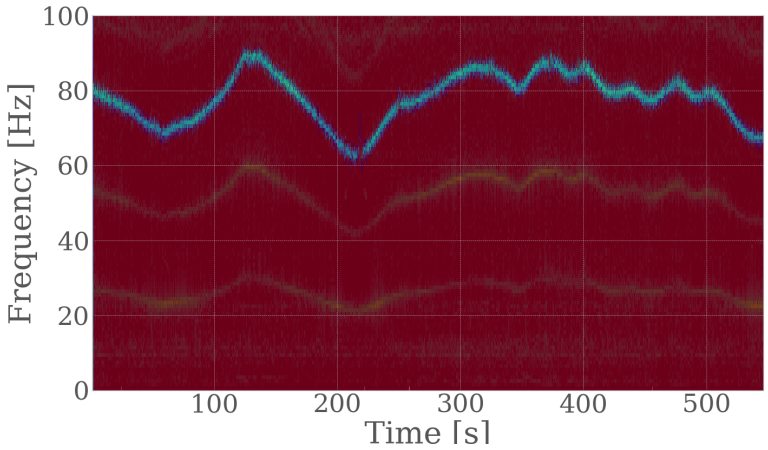

Figure 8: Cost map of the CMMNO data as calculated by the maximum tracking algorithm using a penalized unconstrained cost function.

speed signal measured by the angle encoder in Fig. 9. It can be seen that most methods per-

form quite well in tracking the overall profile of the speed. The cepstrum-based approach shows the largest discrepancies to the encoder speed. This is mainly attributable to the poor quefrency resolution and the fact that not all rhamonics are as well-pronounced as their harmonic spectral counterparts since the cepstrum is strongly influenced by noise. The maximum tracking and VKF approach exhibits one major deviation of the encoder speed around 217 seconds. This deviation is primarily due to the maximum tracking being influenced by a very short, sudden drop in energy of the tracked harmonic. This is also the main problem of this method. If the noise is too high, if there are crossing orders, or if there is a short drop in the amplitude of the tracked harmonic, the maximum tracking can jump quickly to the wrong frequency bins and this is not always straightforward to control in an automated manner.

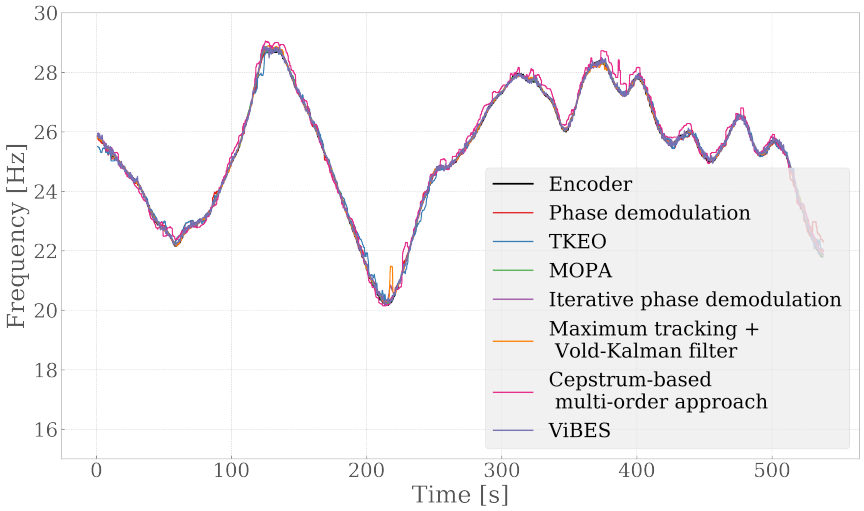

Figure 9: Estimated instantaneous speed profiles of every method on the CMMNO data.

Since it is fairly difficult to assess the accuracy of each method visually in this manner, the mean and median absolute errors are calculated and displayed in Fig. 10. In general, the errors are quite low apart from the one of the cepstrum-based MOPA as is explained earlier. The best result is obtained by the standard MOPA, closely followed by iterative phase demodulation and the maximum tracking with Vold-Kalman filtering. The main reason why the spectrum-based MOPA works so well is thanks to the well-defined harmonic structure in the spectrogram and the large number of different harmonic orders that do not overlap excessively. Averaging the resulting pdfs together of over 60 harmonics produces a very accurate and smooth result. The ViBES method only performs a tiny bit worse than MOPA which is probably due to the difference in implementation and the different harmonic orders chosen. It comes as no surprise that the iterative phase demodulation performs better than the single step phase demodulation and TKEO. The latter mainly suffers from the fact that a fixed window size was chosen for the entire signal. These methods would get closer to the result of the iterative demodulation if custom window sizes and filter bandwidths were defined for every signal part depending on the speed fluctuation. The iterative phase demodulation does not suffer from this drawback since after the first angular resampling it is possible to define a filter bandwidth for the entire signal at once. A similar reasoning can be followed for the VKF approach since after the VKF the signal is essentially a mono-component signal, meaning that phase demodulation of the full-bandwidth signal is possible.

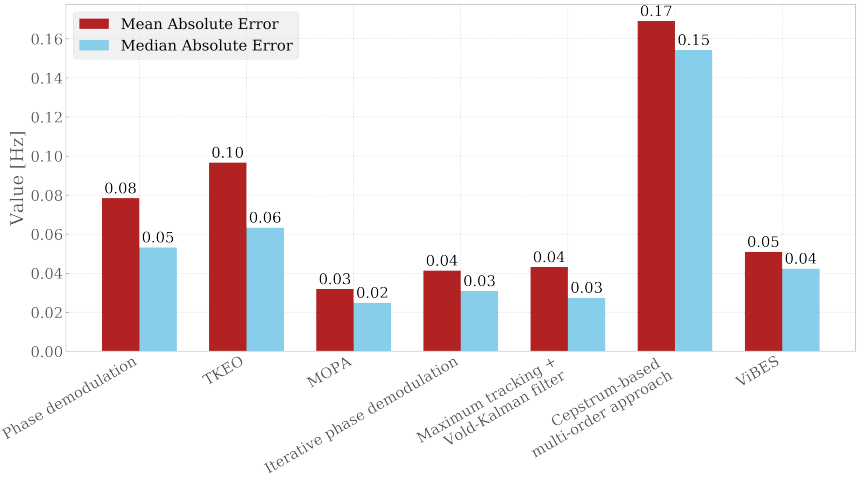

Figure 10: Mean and median absolute errors for every method on the CMMNO data using the encoder as reference.

To provide some insight into the computational effort required by the seven methods, the execution time of every method is returned in Fig. 11. All the computations were done on the same computer using single threaded computation on one CPU core of an i5-5300U processor with 16GB of RAM. Deriving all the computational complexities of every single method is not the main focus of this paper, but Fig. 11 aims to present a ballpark indication of the computation time such that individuals who are interested in implementing a fast speed estimation method have something to judge from.

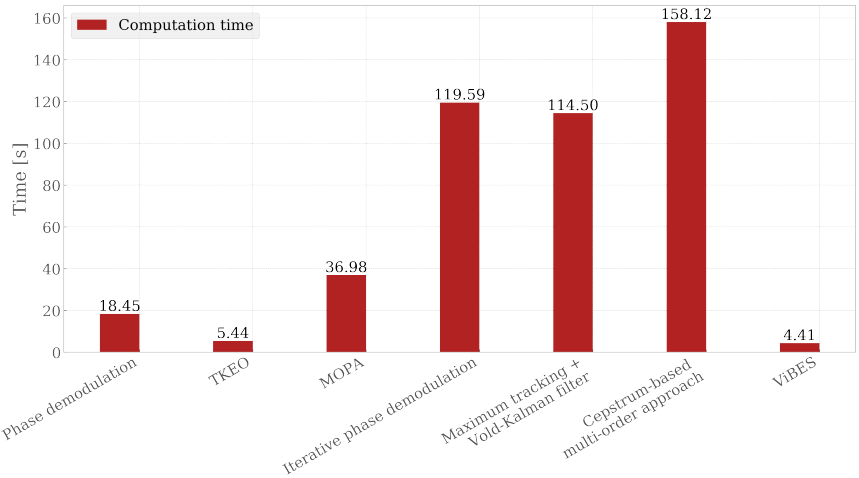

Figure 11: Computation time for every algorithm on the CMMNO data.

3.2. Aircraft engine data

The second data set to be analyzed originates from the Safran contest at the Surveillance 8 conference, held in Roanne, France [55]. The provided data consists of vibration and tachometer signals acquired during a ground test campaign on a civil aircraft engine with two damaged bearings.

A general overview of the engine with the damaged bearings and the sensors locations is displayed

in Fig. 12. The engine has two main shafts and an accessory gearbox with equipment such as pumps, filters, alternators, and starter. The accessory gearbox is linked to the high-pressure shaft HP by a radial drive shaft RDS and a horizontal drive shaft HDS. The kinematics of the gearbox and the rotating speeds of its shafts are described in Fig. 12. A spectrogram of the analyzed signal of accelerometer 2 can be seen in Fig. 14. It is generated using a Hanning window with a length of 2^{11} samples with an overlap of 95%.

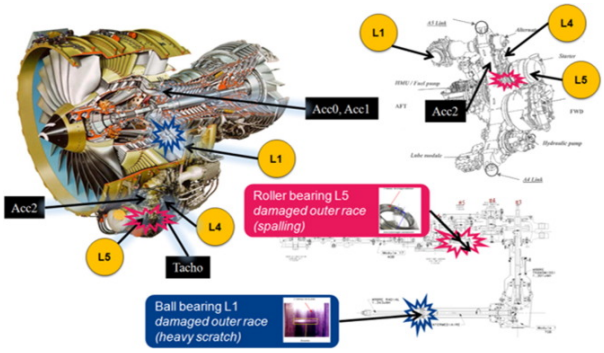

Figure 12: General overview of the engine and the accessory gearbox. Shafts are identified by labels in amber color.

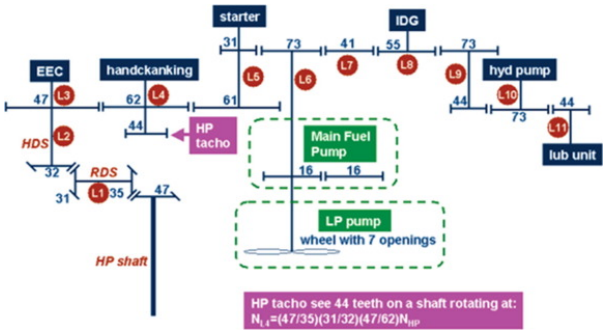

Figure 13: Diagram of the kinematics of the gearbox.

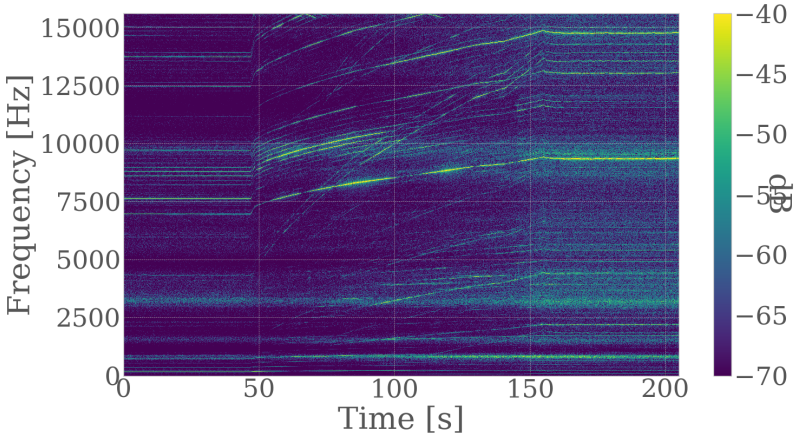

Figure 14: Spectrogram of the analyzed Surveillance 8 aircraft engine vibration data.

3.2.1. Parameter settings

The main harmonic used for the phase demodulation techniques is the 38^{th} harmonic of the high-pressure shaft. The chosen window size is only 1 second due to the very rapid speed increase. The bandwidth is therefore also quite large at 100 Hz. The parameters for MOPA are as follows:

- harmonics orders used: first 60 harmonics of the HP shaft & L1 shaft
- $\{\omega_{min}, \omega_{max}\} = \{175 \text{ Hz}, 230 \text{ Hz}\}$
- $N_w = N_{FFT} = 2^{14}$
- $N_{overlap} = 0.9N_w$
- $K_w = 20$

Table 4: Overview of the input parameters for the Surveillance 8 aircraft engine data set

Method name						
Phase demodulation	Iterative demodulation	TKEO	MOPA	ViBES	Cepstrum-based MOPA	maximum tracking+VKF
ω_{init} = 6960 Hz Bw = 100 Hz $N_w = 2^{14}$	ω_{init} = 6960 Hz Bw = 100 Hz $N_w = 2^{14}$ $\{H_i\} = \{38, 75\}$	ω_{init} = 6960 Hz Bw = 100 Hz $N_w = 2^{14}$	ω_{min} = 175 Hz ω_{max} = 230 Hz $\{H_i\} = \{1, 1.342\}$ N_w=2^{14} $N_{FFT} = 2^{14}$ $N_{overlap}$=90% K_w = 20 $\gamma = 0.4\frac{Hz}{s}$	ω_{init} = 178 Hz $N_{FFT} = 2^{15}$ $N_{overlap}$=90% N_w=31200 $\{R\}$ = {[0.9375, 1.0625], [1.8750, 2.1250], [2.8125, 3.1875], [3.7500, 4.2500], [4.6875, 5.3125], [5.6250, 6.3750], [6.5625, 7.4375], [7.5000, 8.5000]} $\{Z\} = \{\}$ σ_b^2=[ ] σ_l^2=[ ]	ω_{min} = 175 Hz ω_{max} = 230 Hz $\{H_i\} = \{1, 1.342\}$ N_w=2^{14} $N_{FFT} = 2^{14}$ $N_{overlap}$=90% K_w= 20 $\gamma = 0.4\frac{Hz}{s}$	ω_{init} = 6960 Hz Bw_{max}=50Hz $N_w = 2^{14}$ $N_{FFT} = 2^{14}$ $N_{overlap}$=90% N_p=1 N_m=5 Bw_{VKF}=4Hz N_{VKF}=2

- $\gamma = 0.4$

The mesh ranges for the ViBES method were set to correspond to the fundamental through 8th harmonic of the vibration created by the HP shaft. Table 4 displays all of the input parameter settings for this case. The main differences are the different harmonic orders and the adjustments necessary to deal with the very rapid speed increase.

3.2.2. Results

Figure 15 shows the obtained pdf map after summation and continuity introduction for the fundamental speed interval on the Surveillance 8 aircraft engine data. The instantaneous speed profile is again obtained by taking the expected value of every pdf at every time step. It can be seen from the continuity map that the very sudden increase in rotation speed around 50 seconds causes the certainty of the extracted expected value to decrease due to the smearing of all the harmonics, illustrated by the vertical red line.

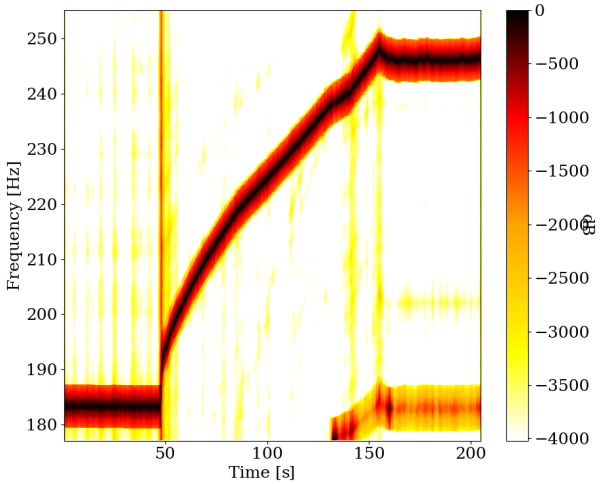

Figure 15: pdf map of the speed profile based on the Surveillance 8 spectrogram after continuity introduction.

Figure 16 displays the cepstrogram. The obtained pdf map after continuity introduction, as shown in Fig. 7, portrays quite clearly the instantaneous speed profile, but suffers from the same

problems as the spectrum-based MOPA around 50 seconds.

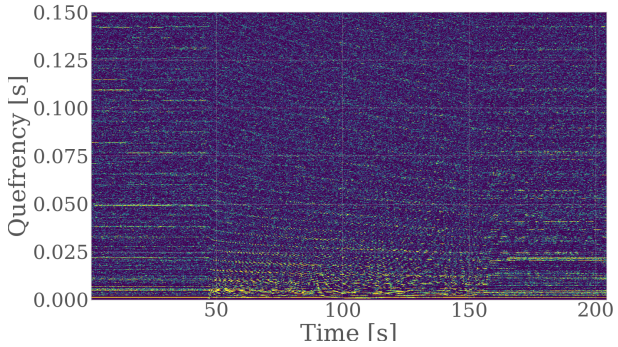

Figure 16: Cepstrogram of the Surveillance 8 aircraft engine data.

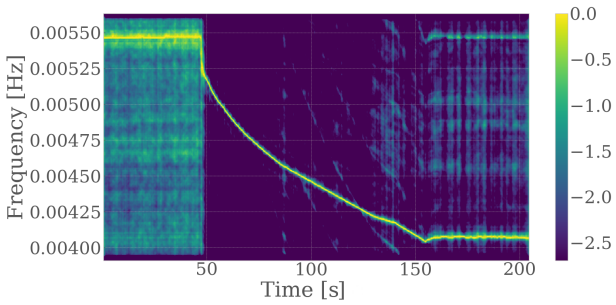

Figure 17: pdf map of the speed profile based on the Surveillance 8 cepstrogram after continuity introduction.

Figure 18 shows the cost map for the Surveillance 8 data as an overlay in red over the spectrogram in the background. The cost map is red where the cost is very high and becomes more transparent where the cost is low. The cost is lowest around the 38^{th} harmonic of the HP shaft frequency illustrated by the visibility of the spectrogram coloring from 6.9 kHz to 9.3kHz.

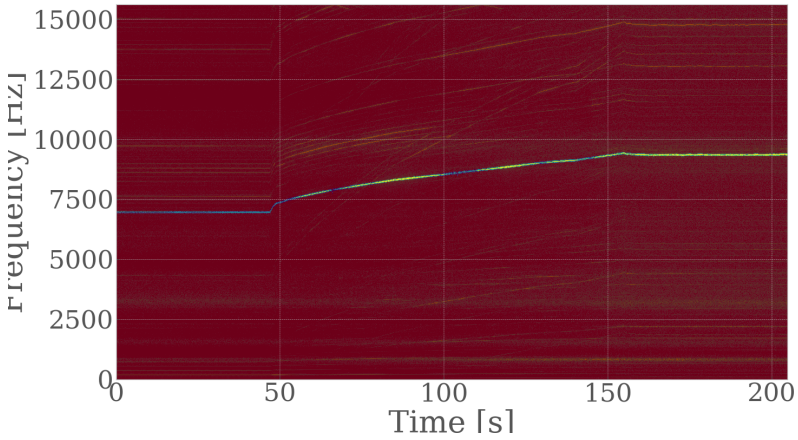

Figure 18: Cost map of the Surveillance 8 data as calculated by the maximum tracking algorithm using a penalized unconstrained cost function.

A comparison of the estimated speed profiles is provided in Fig. 19. All methods are again successful in estimating the general outline of the speed, albeit with varying degree of accuracy. The cepstrum-based MOPA again suffers from resolution issues causing the estimated speed to be quite choppy. The TKEO method manages to track the speed very well visually but suffers from a temporary drop in amplitude and thus signal-to-noise ratio of the 38^{th} harmonic around 105 seconds.

Again the mean and median absolute errors are calculated and shown in Fig. 20 to assess the performance more objectively. The cepstrum-based MOPA performs the worse, which is expected when looking at the speed profiles. Interestingly, the phase demodulation methods perform the best. This can probably be explained by the fact that the 38^{th} & 75^{th} harmonic have a very high

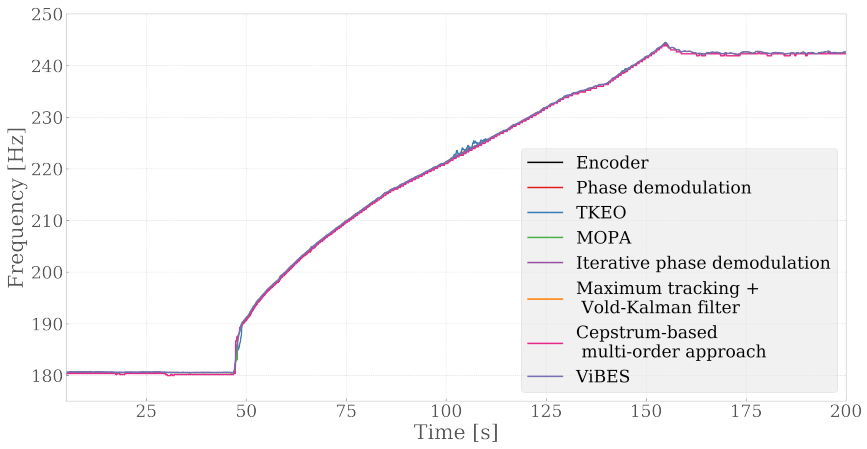

Figure 19: Estimated instantaneous speed profiles of every method on the Surveillance 8 aircraft engine data.

signal-to-noise ratio overall and do not have any significant crossing orders, leading to very clean demodulation results. The TKEO method also has a very low median absolute error but has a large mean error due to the erroneous tracking around 105 seconds. This is most likely attributable to the required differentiation in the method. This is done by a multiplication of the filter band with $j\omega$ at quite high frequencies of around 8 kHz in this case, which means that it increases the noise too. Another observation experienced during the testing of the methods based on the spectrogram is that the resulting errors were quite sensitive to the choice of the set of harmonic orders, more so than for the CMMNO case. Increasing the set of harmonic orders did not always yield a better result than simply choosing the highest amplitude orders, suggesting order set optimization.

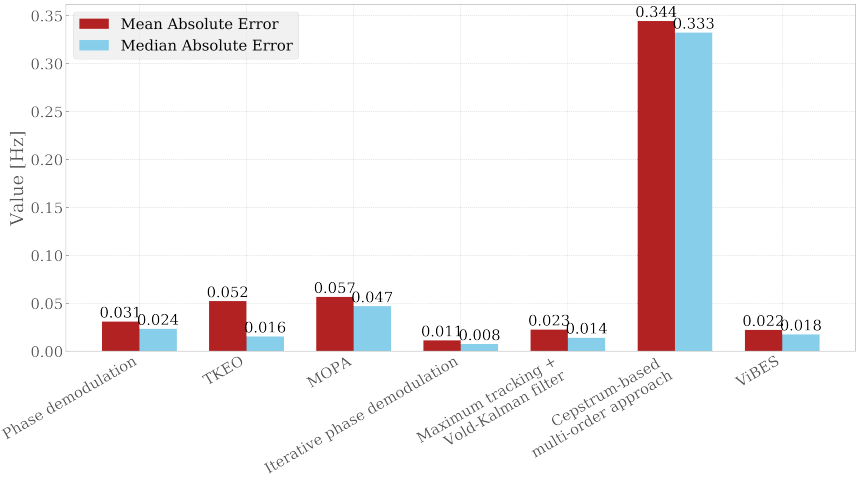

Figure 20: Mean and median absolute errors for every method on the Surveillance 8 data using the encoder as reference.

Lastly, the computation times are displayed in Fig. 21. The calculation of the cost map for the maximum tracking is the main contributor for the maximum tracking with VKF combination, due to the large size of the spectrogram.

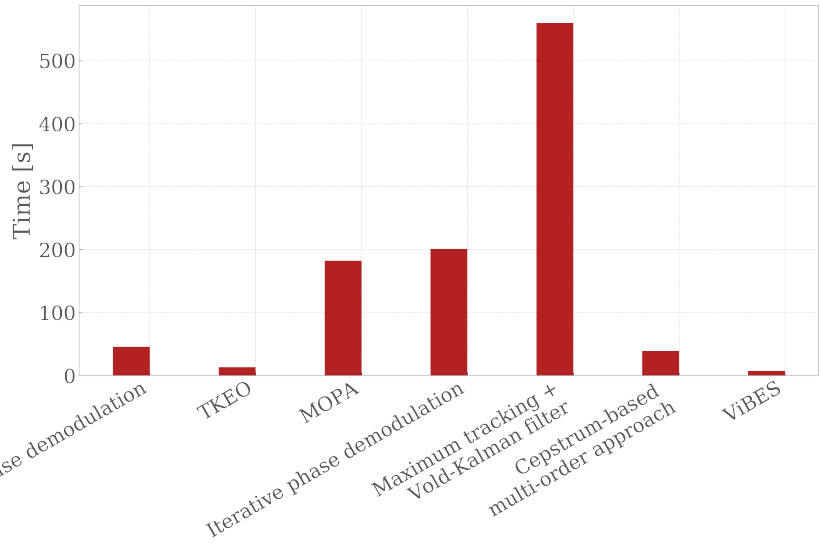

Figure 21: Computation time for every algorithm on the Surveillance 8 data.

3.3. Ship generator data

The third and last data set to be examined is measured on one of the main generators of a YP-700 US navy ship as seen in Fig. 22. Each Yard patrol craft has two generators but only one runs at a time. The generator, shown in Fig. 23, is a Detroit Diesel 3-71 and has a power output of 50 kW at 450 V_{AC}. The electrical system is a three-phase system at 60 Hz. The cause for the excessive speed fluctuation of the generator is a bad governor, displayed in Fig. 24. An accelerometer was placed close to the base of the generator as shown in Fig. 25. The used measurement is approximately 200 seconds in duration at a sample rate of 5 kHz. Interestingly, it contains two fast run-downs and one very fast run-up. These extreme speed fluctuations form quite a significant hurdle to overcome for most of the speed estimation methods as there is also a complete standstill part in-between the first run-down and run-up. The spectrogram of the signal is shown in Fig. 26 and exhibits a large amount of speed-related harmonics. Regrettably, there is no angle encoder or speed reference available for this data set. Therefore a quantitative assessment of estimation errors is not possible, but the authors do believe that highlighting the potential issues that come into play when analyzing this type of data is of some importance to investigate.

3.3.1. Parameter settings

Since there is no reference speed, only the single stage phase demodulation is performed. The input parameters are shown in Table. 5. For the demodulation the first harmonic of the generator shaft is tracked which stays always just below the electrical line frequency of 60 Hz. The MOPA method takes into account the sub-harmonics of the fundamental frequency at multiples of one third its frequency. The mesh ranges for the ViBES method were set to correspond to the first seven components of the vibration spectrum that are correlated to the generator shaft speed. The ViBES method applies the additional adaptations explained in Section 2.5 in the analysis of the ship generator data. The first adaptation, related to the "illegal" frequency regions, is applied by defining $\mathbf{Z}$. $\mathbf{Z}$ contains two regions, $\mathbf{z}_1 = [58.5, 61.5]$ Hz and $\mathbf{z}_2 = [178.5, 181.5]$ Hz. These "illegal" regions of the vibration spectrum contain disturbances corresponding to the fundamental and third harmonic of the electrical line frequency, respectively. Also the second adaptation, related to the wait-and track-mode, is employed. The thresholds are set to $\sigma_l^2 = 0.2$ Hz^2 and $\sigma_h^2 = 0.4$ Hz^2.

Figure 22: Navy ship on which the generator is installed.

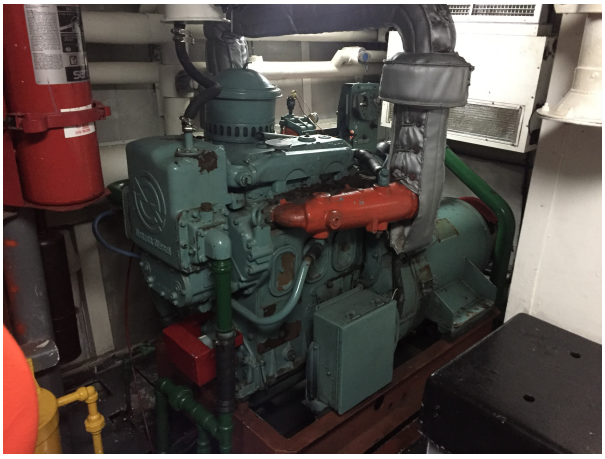

Figure 23: Generator.

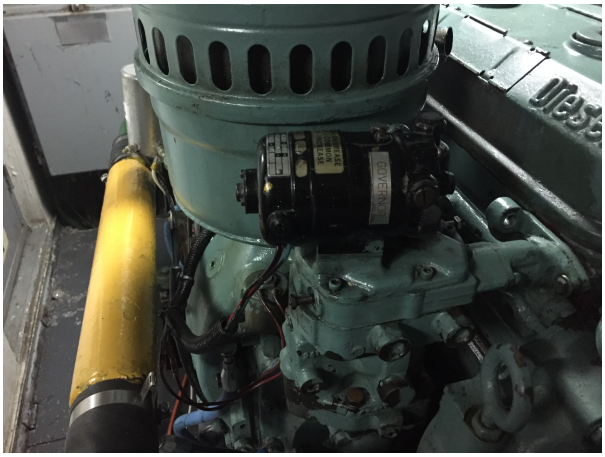

Figure 24: Faulty governor.

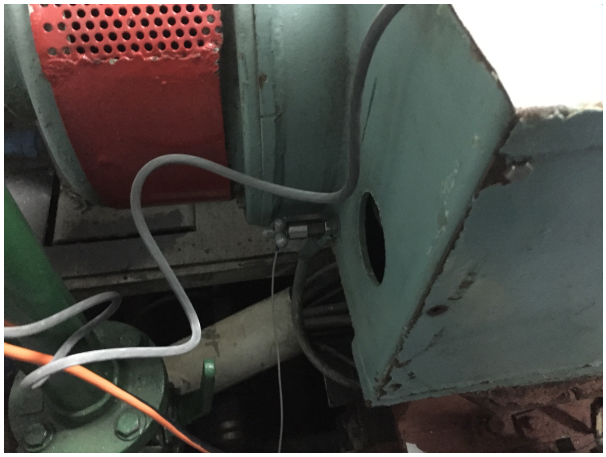

Figure 25: Accelerometer placement.

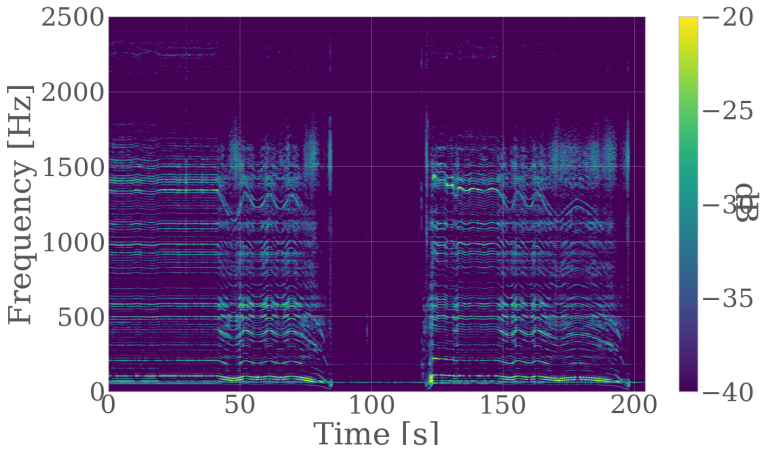

Figure 26: Spectrogram of the analyzed ship generator vibration data.

Table 5: Overview of the input parameters for the ship generator data set

Method name					
Phase demodulation	TKEO	MOPA	ViBES	Cepstrum-based MOPA	maximum tracking+VKF
$\omega_{init} = 53$ Hz $Bw = 10$ Hz $N_w = 5000$	$\omega_{init} = 53$ Hz $Bw = 10$ Hz $N_w = 5000$	$\omega_{min} = 12$ Hz $\omega_{max} = 60$ Hz $\{H_i\} = \{0.333\}$ N_w=5000 $N_{FFT} = 5000$ $N_{overlap}$=98% $K_w = 20$ $\gamma = 0.4\frac{Hz}{s}$	$\omega_{init} = 53$ Hz $N_{FFT} = 2^{13}$ $N_{overlap}$=96% N_w=5000 $\{R\}$= $\{[0.9444, 1.0556]$, $[1.2593, 1.4074]$, $[1.5741, 1.7593]$, $[1.8889, 2.1111]$, $[2.2037, 2.4630]$, $[2.5185, 2.8148]$, $[2.8333, 3.1667]\}$ $\{Z\}$=$\{[58.5, 61.5]$, $[178.5, 181.5]\}$ σ_h^2=$0.4Hz^2$ σ_l^2=$0.2Hz^2$	$\omega_{min} = 12$ Hz $\omega_{max} = 60$ Hz $\{H_i\} = \{0.333\}$ N_w=2^{14} $N_{FFT} = 2^{14}$ $N_{overlap}$=90% K_w= 20 $\gamma = 0.4\frac{Hz}{s}$	$\omega_{init} = 53$ Hz $Bw_{max} = 3$ Hz $N_w = 5000$ $N_{FFT} = 5000$ $N_{overlap}$=99% N_p=1 N_m=5 Bw_{VKF}=3Hz N_{VKF}=2

3.3.2. Results

The run-down and run-up approximately in the middle of the data record make it difficult for some of the techniques to track the speed of the signal in one go, at least not without some additional measures like for example the second adaptation of the ViBES method in Section 2.5. The second adaptation of the ViBES method allows the algorithm to track the second region of operation starting at the 123 second mark after losing tracking of the first operation after 82 seconds. Since the demodulation methods require an initial speed estimate to start tracking a harmonic, this leads to erroneous results when these methods try to track the run-up again due to the standstill in-between causing the tracking to go haywire. Therefore, the data is processed in two separate parts for the phase demodulation, TKEO and maximum tracking method. The MOPA method does not have this drawback because only a speed interval needs to be defined and it automatically gets back "on track" the moment the most likely speed estimate emerges within that speed interval again. This property is usually sufficient for most cases since the focus is mostly on the operating regimes at higher rotation speeds as there is often little to learn from near standstill data from a fault monitoring perspective.

The cepstrogram is shown in Fig. 27 together with the generated pdf map after continuity introduction in Fig. 28. As expected, the probability density functions jump around in frequency due to smearing during the standstill part around 100 seconds and at the end of the record after the run-down. The maximum tracking is done in two separate parts due to the necessity for an initial frequency estimate and the inability of the method to track the very fast run-up at 120 seconds. This run-up goes from 0 Hz to 55 Hz in approximately 4 seconds which causes all the harmonics to smear together in the spectrogram, making maximum tracking practically impossible. The same issue occurs for the phase demodulation methods since the signal has a low SNR in the beginning of the run-up and due to the difficulty in defining a proper band-pass filter. Figure 29 & 30 display the cost maps for the first and second part of the signal on the fundamental harmonic order. This order is chosen because it is reasonably well separated from the other harmonics and the deceleration of the run-down is not too extreme as compared to higher harmonics.

Unfortunately, there was no reference speed provided with these measurements, so only a qualitative visual assessment of the speed profiles can be made. Figure 31 shows the estimated speed profiles and it distinctly showcases the issues that arise when a fast run-down or run-up occurs. The MOPA method is able to continuously track the speed but produces meaningless results during the standstill. The phase demodulation method, maximum tracking with VKF,

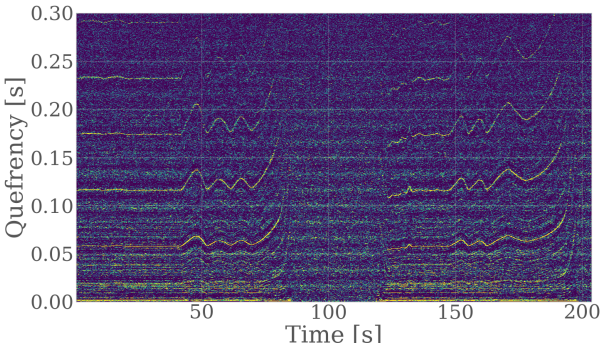

Figure 27: Cepstrogram of the ship generator data.

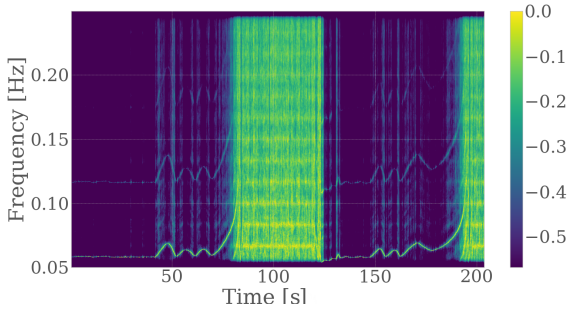

Figure 28: pdf map of the speed profile based on the ship generator cepstrogram after continuity introduction.

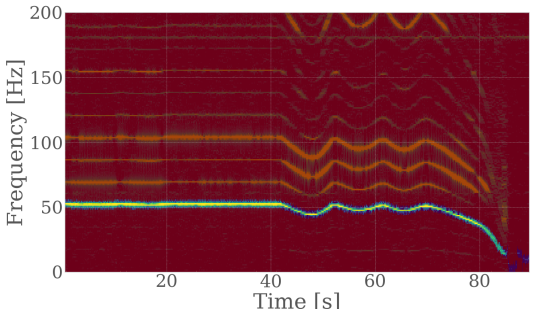

Figure 29: Cost map of the first part of the ship generator data as calculated by the maximum tracking algorithm using a penalized unconstrained cost function.

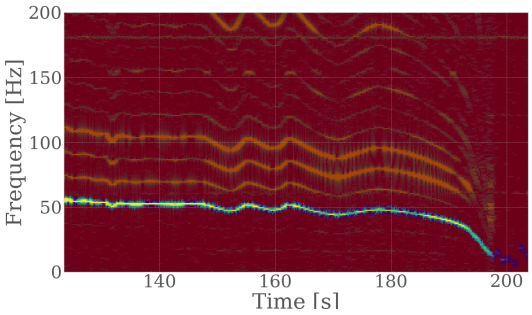

Figure 30: Cost map of the second part of the ship generator data as calculated by the maximum tracking algorithm using a penalized unconstrained cost function.

and TKEO method are unable to track the speed in one go, but perform better in tracking the run-down than MOPA as they produce a sensible result down to 18 Hz approximately. Clearly, the methods based on tracking a specific harmonic within a frequency band need additional built-in intelligence in order to make them cope with sudden run-downs and run-ups as this would make them more flexible to use in an industrial setting.

4. Discussion

There is no absolute outcome as in which method is the most accurate for every case and which method is always the easiest to use. Nevertheless, some general comments can be made.

The signal-to-noise ratio, with the harmonics being the signal and all the other signal content being the noise, logically influences all the speed estimation methods mentioned in this paper. The methods that are based on a single harmonic are more dependent on the signal having a high SNR and well-separated harmonic as compared to the multi-harmonic methods. Therefore, in situations where there is not a single harmonic that is well excited, the multi-harmonic methods should outperform the single harmonic methods due to a reduction in variance by taking into account multiple harmonics.

The phase demodulation method produces very satisfactory results as long as there is a high SNR harmonic present in the signal without any significant crossing orders and well separated from nearby harmonics. Doing an additional step of angular resampling and phase demodulation of a higher harmonic order can improve the result even further but the limit of the accuracy gain

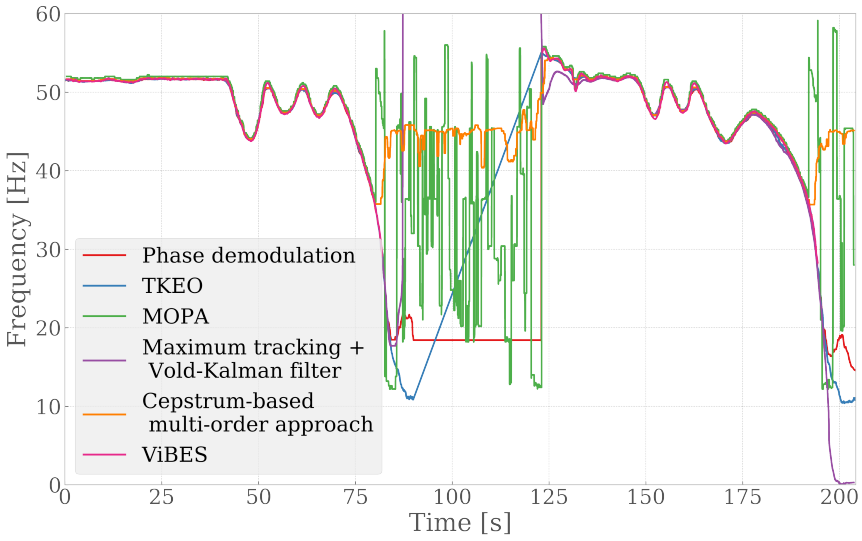

Figure 31: Estimated instantaneous speed profiles on the ship generator data.

is usually reached after one to two iterations. The downside to these methods is the need for an initial speed estimate. This means that when there is a total standstill such as in the third data set, the phase demodulation methods fail to start tracking the right harmonic again by themselves since they have been demodulating noise during the standstill. This could be improved by adding some intelligence to the tracking such as described by the variance-based lock-in tracking adaptation in Section 2.5. The same remarks are valid for the TKEO method. This method also seems to suffer slightly from noise amplification at high frequencies due to the differentiation involved.

The methods based on a TFR or TQR of the signal are able to continuously track the speed since they estimate the most likely speed at every time index. The performance of the cepstrum-based MOPA is consistently the worst due to the poor resolution and sensitivity to noise, but it is easy to use since the harmonic orders are usually known a priori from the kinematics of the investigated system. The spectrum-based MOPA and ViBES method are two similar takes on perceiving the spectrogram as a probability density function map, but with different implementations and adaptations. The accuracy is very similar for both methods and depends mostly on the chosen inputs. The main drawback of this type of techniques is the dependency on the frequency and time resolution of the TFR or TQR. If the speed fluctuates very strongly, the harmonics tend to smear together in the short-time spectrum making it difficult to distinguish them and causing the obtained pdfs to be smeared as well. It is also difficult to capture small, but fast speed fluctuations since the time resolution is often too coarse to identify such variations. In the future a possibility to automate this search for the optimal window length choice will be investigated. An optimization procedure could be implemented that can for example be based on the maximum acceleration of the speed or be based on a statistical quantity of the time-frequency representation. Another potential improvement would be to remove the a-priori assumption about the maximum physically possible speed acceleration. Instead, the maximum acceleration could be tracked and updated over time based on the previous time windows. The idea here is to make the Gaussian pdfs as narrow as possible for each time step.

The combination of the maximum tracking and the Vold-Kalman filter tries to circumvent this

issue by using the VKF as a time-varying band-pass filter such that the phase can be obtained from the resulting analytic signal. The main issue however in utilizing the VKF is the large number of adjustable parameters that can impact significantly the performance of the method. This encumbers somewhat the practicality of the approach and makes it probably the most complex technique out of the seven tested. Also the maximum tracking used in this paper is based on calculating a cost map of the spectrogram which can take quite a while to calculate and needs an initial speed estimate. A potential improvement can probably be made by combining a technique such as MOPA with a time-varying band-pass filter such as the VKF.

Finally, if there is no tacho or angle encoder available to compare the estimated speed to, then the only sources of information available are the estimated speed signal itself and the vibration signal. It is reasonable to assume that the speed profile needs to be continuous and cannot be jumping around like e.g. in Fig.31. A possible way to grade the estimation therefore could be based on the acceleration of the speed signal. The vibration signal can also be employed: if for example the RMS of the signal drops below a certain threshold, you can assume the machine is in standstill condition and thus the estimated speed can be ignored. Such approaches offer a more automated way of assessing the quality of the estimated speed compared to visually inspecting it.

5. Conclusion

This paper investigates seven different instantaneous angular speed estimation methods based on the most commonly used principles, namely signal demodulation and tracking in a time-frequency representation of the vibration signal. It is clear from Section 1 that there exists a large number of possible variations and extensions to these two basic techniques. While it is impossible to investigate all of these variations, this paper aims to shed some light on the strengths and drawbacks of different method implementations by assessing their performance on experimental data. A short overview of the different theoretical backgrounds of each method is provided in Section 2. Three experimental vibration data sets are investigated: one was measured on a wind turbine gearbox, one on an aircraft engine, and one on the generator of a ship. Section 3 discusses the results obtained by applying the seven methods on these three data sets. While every method is able to track the general speed profile for each case, the level of manual involvement in tweaking the input parameters for every method differs greatly, as does the resulting accuracy. The performance of every method is discussed in Section 4. Based on the assessment provided in this paper, it is evident that effective speed estimation methods already exist, but that there are still improvements to be made. The main challenges for speed estimation methods continue to be sudden fast speed fluctuations, operating regime changes that influence the harmonic structure, and accurate continuous tracking, even at low speeds.

6. Acknowledgment

The authors of VUB would like to thank FWO for their support with an SB Ph.D. fellow grant and the agency for Innovation by Science and Technology in Belgium for supporting the SBO HYMOP project and the Fulbright foundation for facilitating collaboration with MIT. They would also like to thank FWO for providing funding for a long stay abroad of Cédric Peeters at the university of INSA Lyon. The authors of MIT & the US Naval Academy would like to acknowledge the support of the Grainger Foundation, the MIT-ExxonMobil collaboration through the MIT Energy Initiative, and the Office of Naval Research Structural Acoustics Program. The authors are also grateful to the organizers of the CMMNO and Surveillance conference for making the experimental data sets available to the public.

References

[1] A. K. Jardine, D. Lin, D. Banjevic, A review on machinery diagnostics and prognostics implementing condition-based maintenance, Mechanical systems and signal processing 20 (7) (2006) 1483–1510.

[2] P. Tchakoua, R. Wamkeue, M. Ouhrouche, F. Slaoui-Hasnaoui, T. A. Tameghe, G. Ekemb, Wind turbine condition monitoring: State-of-the-art review, new trends, and future challenges, Energies 7 (4) (2014) 2595–2630.

[3] D. Rémond, J. Antoni, R. Randall, Editorial for the special issue on instantaneous angular speed (ias) processing and angular applications, Mechanical Systems and Signal Processing 1 (44) (2014) 1–4.

[4] R. Potter, A new order tracking method for rotating machinery, Sound and Vibration 24 (9) (1990) 30–34.

[5] K. Fyfe, E. Munck, Analysis of computed order tracking, Mechanical Systems and Signal Processing 11 (2) (1997) 187–205.

[6] K. Wang, P. S. Heyns, Application of computed order tracking, vold–kalman filtering and emd in rotating machine vibration, Mechanical Systems and Signal Processing 25 (1) (2011) 416–430.

[7] H. Kim, Y. Yamakawa, T. Senoo, M. Ishikawa, Visual encoder: robust and precise measurement method of rotation angle via high-speed rgb vision, Optics Express 24 (12) (2016) 13375–13386.

[8] A. Collet, M. Martinez, S. S. Srinivasa, The moped framework: Object recognition and pose estimation for manipulation, The International Journal of Robotics Research 30 (10) (2011) 1284–1306. arXiv:https://doi.org/10.1177/0278364911401765, doi:10.1177/0278364911401765.
URL https://doi.org/10.1177/0278364911401765

[9] D. G. Lowe, Distinctive image features from scale-invariant keypoints, International journal of computer vision 60 (2) (2004) 91–110.

[10] H. Bay, A. Ess, T. Tuytelaars, L. Van Gool, Speeded-up robust features (surf), Computer vision and image understanding 110 (3) (2008) 346–359.

[11] Y.-s. Kwon, W.-j. Kim, Development of a new high-resolution angle-sensing mechanism using an rgb sensor, IEEE/ASME Transactions on Mechatronics 19 (5) (2014) 1707–1715.

[12] T. Suzuki, T. Endo, O. Sasaki, J. E. Greivenkamp, Two-dimensional small-rotation-angle measurement using an imaging method, Optical Engineering 45 (4) (2006) 043604.

[13] W. Li, J. Jin, X. Li, B. Li, Method of rotation angle measurement in machine vision based on calibration pattern with spot array, Applied optics 49 (6) (2010) 1001–1006.

[14] K.-M. Lee, D. Zhou, A real-time optical sensor for simultaneous measurement of three-dof motions, IEEE/ASME Transactions on Mechatronics 9 (3) (2004) 499–507.

[15] T. Kadowaki, K. Kobayashi, K. Watanabe, Rotation angle measurement of high-speed flying object, in: SICE-ICASE, 2006. International Joint Conference, IEEE, 2006, pp. 5256–5259.

[16] J. Zhong, S. Zhong, Q. Zhang, N. Maia, Y. Shen, S. Liu, Y. Yu, Z. Peng, Vision-based system for simultaneous monitoring of shaft rotational speed and axial vibration using non-projection composite fringe pattern, Mechanical Systems and Signal Processing 120 (2019) 765–776.

[17] Y. Wang, L. Wang, Y. Yan, Rotational speed measurement through digital imaging and image processing, in: Instrumentation and Measurement Technology Conference (I2MTC), 2017 IEEE International, IEEE, 2017, pp. 1–6.

[18] T. Wang, L. Wang, Y. Yan, S. Zhang, Rotational speed measurement using a low-cost imaging device and image processing algorithms, in: 2018 IEEE International Instrumentation and Measurement Technology Conference (I2MTC), IEEE, 2018, pp. 1–6.

[19] Q. L. Hugo Andre, Ilyes Khelf, Harmonic product spectrum revisited and adapted for rotating machine monitoring based on ias, in: Surveillance9, 2017.

[20] L. Renaudin, F. Bonnardot, O. Musy, J. Doray, D. Rémond, Natural roller bearing fault detection by angular measurement of true instantaneous angular speed, Mechanical Systems and Signal Processing 24 (7) (2010) 1998–2011.

[21] A. Yousef Ben Sasi, F. Gu, B. Payne, A. Ball, Instantaneous angular speed monitoring of electric motors, Journal of Quality in Maintenance Engineering 10 (2) (2004) 123–135.

[22] J. Urbanek, T. Barszcz, N. Sawalhi, R. Randall, Comparison of amplitude-based and phase-based methods for speed tracking in application to wind turbines, Metrology and measurement systems 18 (2) (2011) 295–304.

[23] H. K. Kwok, D. L. Jones, Improved instantaneous frequency estimation using an adaptive short-time fourier transform, IEEE transactions on signal processing 48 (10) (2000) 2964–2972.

[24] S. Cheung, J. S. Lim, Combined multiresolution (wide-band/narrow-band) spectrogram, IEEE Transactions on signal processing 40 (4) (1992) 975–977.

[25] Z. Peng, G. Meng, F. Chu, Z. Lang, W. Zhang, Y. Yang, Polynomial chirplet transform with application to instantaneous frequency estimation, IEEE Transactions on Instrumentation and Measurement 60 (9) (2011) 3222–3229.

[26] S. C. Sekhar, T. Sreenivas, Effect of interpolation on pwvd computation and instantaneous frequency estimation, Signal processing 84 (1) (2004) 107–116.

[27] K. C. Gryllias, I. A. Antoniadis, Estimation of the instantaneous rotation speed using complex shifted morlet wavelets, Mechanical Systems and Signal Processing 38 (1) (2013) 78–95.

[28] J. M. Aller, T. G. Habetler, R. G. Harley, R. M. Tallam, S. B. Lee, Sensorless speed measurement of ac machines using analytic wavelet transform, IEEE Transactions on Industry Applications 38 (5) (2002) 1344–1350.

[29] I. Daubechies, J. Lu, H.-T. Wu, Synchrosqueezed wavelet transforms: A tool for empirical mode decomposition, arXiv preprint arXiv:0912.2437.

[30] F. Auger, P. Flandrin, Improving the readability of time-frequency and time-scale representations by the reassignment method, IEEE Transactions on signal processing 43 (5) (1995) 1068–1089.

[31] K. Kodera, R. Gendrin, C. d. Villedary, Analysis of time-varying signals with small bt values, IEEE Transactions on Acoustics, Speech, and Signal Processing 26 (1) (1978) 64–76.

[32] J. Shi, M. Liang, D.-S. Necsulescu, Y. Guan, Generalized stepwise demodulation transform and synchrosqueezing for time–frequency analysis and bearing fault diagnosis, Journal of Sound and Vibration 368 (2016) 202–222.

[33] Z. Feng, X. Chen, M. Liang, Iterative generalized synchrosqueezing transform for fault diagnosis of wind turbine planetary gearbox under nonstationary conditions, Mechanical Systems and Signal Processing 52 (2015) 360–375.

[34] S. Xi, H. Cao, X. Chen, X. Zhang, X. Jin, A frequency-shift synchrosqueezing method for instantaneous speed estimation of rotating machinery, Journal of Manufacturing Science and Engineering 137 (3) (2015) 031012.

[35] D. Iatsenko, P. V. McClintock, A. Stefanovska, Linear and synchrosqueezed time-frequency representations revisited. part i: Overview, standards of use, related issues and algorithms, arXiv preprint arXiv:1310.7215.

[36] D. Iatsenko, P. V. McClintock, A. Stefanovska, Linear and synchrosqueezed time-frequency representations revisited. part ii: Resolution, reconstruction and concentration, arXiv preprint arXiv:1310.7274.

[37] D. Iatsenko, P. V. McClintock, A. Stefanovska, Linear and synchrosqueezed time–frequency representations revisited: Overview, standards of use, resolution, reconstruction, concentration, and algorithms, Digital Signal Processing 42 (2015) 1–26.

[38] R. F. Barrett, D. A. Holdsworth, Frequency tracking using hidden markov models with amplitude and phase information, IEEE Transactions on Signal Processing 41 (10) (1993) 2965–2976.

[39] S. Schmidt, P. S. Heyns, J. P. De Villiers, A tacholess order tracking methodology based on a probabilistic approach to incorporate angular acceleration information into the maxima tracking process, Mechanical Systems and Signal Processing 100 (2018) 630–646.

[40] I. Djurović, L. Stanković, An algorithm for the wigner distribution based instantaneous frequency estimation in a high noise environment, Signal Processing 84 (3) (2004) 631–643.

[41] S. Wang, X. Chen, Y. Wang, G. Cai, B. Ding, X. Zhang, Nonlinear squeezing time–frequency transform for weak signal detection, signal processing 113 (2015) 195–210.

[42] D. Iatsenko, P. V. McClintock, A. Stefanovska, Extraction of instantaneous frequencies from ridges in time–frequency representations of signals, Signal Processing 125 (2016) 290–303.

[43] R. Zimroz, J. Urbanek, T. Barszcz, W. Bartelmus, F. Millioz, N. Martin, Measurement of instantaneous shaft speed by advanced vibration signal processing-application to wind turbine gearbox, Metrology and Measurement Systems 18 (4) (2011) 701–712.

[44] Q. Leclere, H. André, J. Antoni, A multi-order probabilistic approach for instantaneous angular speed tracking debriefing of the cmmno 14 diagnosis contest, Mechanical Systems and Signal Processing 81 (2016) 375–386.

[45] C. Peeters, Q. Leclre, J. Antoni, P. Guillaume, J. Helsen, Vibration-based angular speed estimation for multi-stage wind turbine gearboxes, Journal of Physics: Conference Series 842 (1) (2017) 012053.
URL http://stacks.iop.org/1742-6596/842/i=1/a=012053

[46] F. Bonnardot, M. El Badaoui, R. Randall, J. Daniere, F. Guillet, Use of the acceleration signal of a gearbox in order to perform angular resampling (with limited speed fluctuation), Mechanical Systems and Signal Processing 19 (4) (2005) 766–785.

[47] J. Urbanek, T. Barszcz, J. Antoni, A two-step procedure for estimation of instantaneous rotational speed with large fluctuations, Mechanical Systems and Signal Processing 38 (1) (2013) 96–102.

[48] F. Combet, L. Gelman, An automated methodology for performing time synchronous averaging of a gearbox signal without speed sensor, Mechanical systems and signal processing 21 (6) (2007) 2590–2606.

[49] A.-O. Boudraa, J.-C. Cexus, F. Salzenstein, L. Guillon, If estimation using empirical mode decomposition and nonlinear teager energy operator, in: Control, Communications and Signal Processing, 2004. First International Symposium on, IEEE, 2004, pp. 45–48.

[50] R. Randall, W. Smith, Use of the teager kaiser energy operator to estimate machine speed, in: Paper to be presented at PHM Europe conference, Bilbao, Spain, 2016, pp. 5–8.

[51] O. Cardona-Morales, L. Avendaño, G. Castellanos-Domínguez, Nonlinear model for condition monitoring of non-stationary vibration signals in ship driveline application, Mechanical Systems and Signal Processing 44 (1-2) (2014) 134–148.

[52] B. F. La Scala, R. R. Bitmead, Design of an extended kalman filter frequency tracker, IEEE Transactions on Signal Processing 44 (3) (1996) 739–742.

[53] F. Combet, R. Zimroz, A new method for the estimation of the instantaneous speed relative fluctuation in a vibration signal based on the short time scale transform, Mechanical Systems and Signal Processing 23 (4) (2009) 1382–1397.

[54] M. D. Coats, R. Randall, Order-tracking with and without a tacho signal for gear fault diagnostics, in: Proceedings of Acoustics, 2012, pp. 1–6.

[55] J. Antoni, J. Griffaton, H. André, L. D. Avendaño-Valencia, F. Bonnardot, O. Cardona-Morales, G. Castellanos-Dominguez, A. P. Daga, Q. Leclère, C. M. Vicuña, et al., Feedback on the surveillance 8 challenge: vibration-based diagnosis of a safran aircraft engine, Mechanical Systems and Signal Processing 97 (2017) 112–144.

[56] D. Hanson, R. Randall, J. Antoni, D. Thompson, T. Waters, R. Ford, Cyclostationarity and the cepstrum for operational modal analysis of mimo systemspart i: Modal parameter identification, Mechanical systems and signal processing 21 (6) (2007) 2441–2458.

[57] D. Iatsenko, P. V. McClintock, A. Stefanovska, On the extraction of instantaneous frequencies from ridges in time-frequency representations of signals, arXiv preprint arXiv:1310.7276.

[58] C. Bishop, Pattern recognition and machine learning, Springer, 2006.

[59] M.-C. Pan, Y.-F. Lin, Further exploration of vold–kalman-filtering order tracking with shaft-speed informationi: Theoretical part, numerical implementation and parameter investigations, Mechanical systems and signal processing 20 (5) (2006) 1134–1154.

[60] J. R. Blough, A survey of dsp methods for rotating machinery analysis, what is needed, what is available, Journal of sound and vibration 262 (3) (2003) 707–720.

[61] J. Tuma, Setting the passband width in the vold-kalman order tracking filter, in: Twelfth International Conference on Sound and Vibration (ICSV12), Lisbon, Portugal, July, 2005, pp. 11–14.